Applied Mathematical Modelling 142 (2025) 115962

Contents lists available at ScienceDirect

Applied Mathematical Modelling

journal homepage: www.elsevier.com/locate/apm

Coupling of non-hydrostatic model with unresolved point-particle model for simulating particle-laden free surface flows

Yuhang Chen [a,b,c], Yongping Chen [a,b,*], Zhenshan Xu [a,b], Pengzhi Lin [d], Zhihua Xie [c,*]

[a] The National Key Laboratory of Water Disaster Prevention, Hohai University, Nanjing, 210098, Jiangsu, China
[b] College of Harbor, Coastal and Offshore Engineering, Hohai University, Nanjing, 210098, Jiangsu, China
[c] School of Engineering, Cardiff University, Queen's Buildings, Cardiff, CF24 3AA, UK
[d] State Key Laboratory of Hydraulics and Mountain River Engineering, Sichuan University, Chengdu, 610065, Sichuan, China

ARTICLE INFO

Keywords:
Non-hydrostatic model
Point-particle
Particle-laden free surface flows

ABSTRACT

Sediment-laden flow is a common phenomenon in nature and the deposition of sediments can make a great difference in landscape formation or marine systems. The complexity of this issue can be further increased with temporal variations in the free surface elevation. This paper aims to present a two-phase flow model that effectively integrates the non-hydrostatic free surface model with the Lagrangian point-particle model. The free surface elevation is conceptualized as a height function and is tracked using a Lagrangian-Eulerian method. This new model is validated by five test cases, showing a good agreement with analytical or experimental results. This demonstrates the model's proficiency in handling sediment-laden flow under various free surface flow conditions, particularly with surface waves. Consequently, the proposed model holds promise for investigating sediment-laden flow issues in coastal regions.

1. Introduction

Sediment-laden free surface flow is a prevalent phenomenon in nature. It is vital for comprehending a range of environmental and geological processes. This interaction, characterized by the movement of water containing sediment particles, significantly influences landscape formation [1,2], river [3,4] and marine ecosystems [5,6]. Understanding the intricate dynamics in sediment-laden flow is essential for both appreciating natural mechanisms and devising practical applications in the fields of environmental engineering and hydrodynamics.

To effectively capture such phenomena, numerical simulation has emerged as an efficient method. Over the past decade, extensive research has been conducted on sediment transport patterns and various numerical models have been utilized. They can be divided mainly into three categories, namely Euler–Euler model [7–12], Euler–Lagrange model [13–16] and Lagrange-Lagrange model [17–22]. The Euler–Euler model treats sediment phase as a continuum and sediment transport is modeled using an advection–diffusion equation. It effectively captures the sediment transport process by solving the mass and momentum equations for both fluid and sediment phases, incorporating closures for interphase momentum transfer, turbulence, and intergranular stresses. However, for polydisperse particles or those particles with greater inertia (Stokes number (St) ≥ 1), such kind of model encounters challenges [23].

* Corresponding authors.
E-mail addresses: ypchen@hhu.edu.cn (Y. Chen), zxie@cardiff.ac.uk (Z. Xie).

https://doi.org/10.1016/j.apm.2025.115962
Received 9 May 2024; Received in revised form 9 January 2025; Accepted 20 January 2025

Available online 22 January 2025

In such circumstances, the Lagrangian approach, where sediment particles are individually tracked via the Maxey–Riley equations [24], offers a more suitable alternative. Apart from the Lagrange-Lagrange model, which treats both fluid and sediment phases as particles, the Euler–Lagrange model can achieve relatively good results with reasonable computational cost. Hence, the Euler–Lagrange model is becoming more and more popular in simulating two-phase flow problems.

The Euler–Lagrange model can be categorized into two main approaches: the fully resolved particle model and the unresolved point-particle approach. As for the fully resolved particle model, the immersed boundary method [25–27] is adopted and no-slip boundary condition is directly enforced on the surfaces of individual particles [28], necessitating a grid size smaller than the sediment diameters to resolve both the particles and the detailed flow fields around them. In that case, the fully resolved particle model has the potential to substantially enhance our understanding of microscale sediment transport processes and foster the development of improved closures for averaged equations [29]. However, the limitations on the computational resources are always a problem for simulating sediment transport at different spatial and temporal scales [23]. By contrast, in the unresolved point-particle model, particles are treated as point sources without resolving the particle–fluid interfaces by the continuous phase grid, allowing for a grid size significantly larger than the sediment diameter. Hence, the grid size in this model can be several times larger than the sediment diameter. Considering its much smaller computational cost, this approach is now well established as a research tool in a number of fields [30–33], which is more suitable for application when a large number of small particles are involved [34].

When simulating sediment-laden flows with free surface elevation changes using the Euler–Lagrange model, the volume-of-fluid (VOF) method [35] is commonly used and has been successfully applied in many conditions [36–39]. This interface capturing method can capture the water surface well although it is constrained by substantial computational demands. In contrast, non-hydrostatic models, which conceptualize the free-surface elevation as a single-valued function dependent on horizontal coordinates, offer an efficient solution for tracking surface movements with reduced computational demands [40]. The key advantage of non-hydrostatic models lies in their ability to accurately predict wave dispersion with relatively few vertical grid points. For example, studies by Lin and Li [41] and Ma et al. [42] have shown that 10–20 vertical layers are sufficient to describe wave dispersion to an acceptable level, even with simplified pressure boundary conditions at the top layer. Further advancements [43,44] enable even more computational efficiency by positioning pressure at the cell faces rather than at the cell centers. Hence, these non-hydrostatic models have been widely used for simulating free-surface flows in both ocean and coastal environments [41–49]. Ma et al. [50] used the non-hydrostatic model - NHWAVE to simulate both turbidity currents and the tsunami wave generation by a landslide. Berard et al. [51] simulated the bathymetry change of a steep sand dune under waves using the XBeach model. Zhang et al. [52] proposed a two-layer coupled model to investigate submarine landslides and resulting tsunami generation over irregular bathymetry. However, in these models, the sediment phase is considered as a continuum and in fact, they are all Euler-Euler models.

It can be seen from the above literature review that contemporary Euler–Lagrange models predominantly utilize a combination of the Navier-Stokes equation and an interface capturing method when applied to sediment-laden flow problems with free surfaces. However, these models generally incur higher computational costs than non-hydrostatic models. Most non-hydrostatic models are based on the Euler-Euler method when simulating particle-laden flows. The integration of non-hydrostatic models with the point-particle model remains relatively rare. It is evident that the fusion of non-hydrostatic models with point-particle models holds significant potential. This approach capitalizes on the relatively lower computational demands of non-hydrostatic models while enhancing the accuracy of transport patterns for particles with greater inertia, as facilitated by the point-particle model.

In this paper, the main novelty is to develop a two-phase flow model which couples the non-hydrostatic free surface model with a Lagrangian point-particle model to simulate dilute sediment-laden free surface flow problems. A series of numerical simulation cases, encompassing regular waves, wave-structure interactions, a single spherical particle settling in stationary and oscillation environment, and sediment-laden jet in stationary and wave environments are conducted to verify the model's applicability. The paper is organized as follows: the governing equation and boundary conditions for the two-phase flow model are introduced in Section 2. The numerical methods are presented in Section 3. Five test cases are validated in Section 4. Finally, the conclusions are given in Section 5.

2. Governing equations

2.1. Continuous phase

A three-dimensional large eddy simulation model developed by Chen et al. [46] was adopted. The governing equations of fluid phase in the non-hydrostatic model are the spatially filtered Navier-Stokes equations, which can be written as:

$$\frac{\partial u_1}{\partial x^*}+\frac{\partial u_2}{\partial y^*}+\frac{\partial u_3}{\partial z^*}=0 \tag{1}$$

$$\frac{\partial u_1}{\partial t^*}+u_1\frac{\partial u_1}{\partial x^*}+u_2\frac{\partial u_1}{\partial y^*}+u_3\frac{\partial u_1}{\partial z^*}=-\frac{1}{\rho_f}\frac{\partial p}{\partial x^*}+g_x+\frac{\partial \tau_{xx}}{\partial x^*}+\frac{\partial \tau_{xy}}{\partial y^*}+\frac{\partial \tau_{xz}}{\partial z^*}-\frac{\partial \tau_{xx}^{SGS}}{\partial x^*}-\frac{\partial \tau_{xy}^{SGS}}{\partial y^*}-\frac{\partial \tau_{xz}^{SGS}}{\partial z^*} \tag{2}$$

$$\frac{\partial u_2}{\partial t^*}+u_1\frac{\partial u_2}{\partial x^*}+u_2\frac{\partial u_2}{\partial y^*}+u_3\frac{\partial u_2}{\partial z^*}=-\frac{1}{\rho_f}\frac{\partial p}{\partial y^*}+g_y+\frac{\partial \tau_{yx}}{\partial x^*}+\frac{\partial \tau_{yy}}{\partial y^*}+\frac{\partial \tau_{yz}}{\partial z^*}-\frac{\partial \tau_{yx}^{SGS}}{\partial x^*}-\frac{\partial \tau_{yy}^{SGS}}{\partial y^*}-\frac{\partial \tau_{yz}^{SGS}}{\partial z^*} \tag{3}$$

$$\frac{\partial u_3}{\partial t^*}+u_1\frac{\partial u_3}{\partial x^*}+u_2\frac{\partial u_3}{\partial y^*}+u_3\frac{\partial u_3}{\partial z^*}=-\frac{1}{\rho_f}\frac{\partial p}{\partial z^*}+g_z+\frac{\partial \tau_{zx}}{\partial x^*}+\frac{\partial \tau_{zy}}{\partial y^*}+\frac{\partial \tau_{zz}}{\partial z^*}-\frac{\partial \tau_{zx}^{SGS}}{\partial x^*}-\frac{\partial \tau_{zy}^{SGS}}{\partial y^*}-\frac{\partial \tau_{zz}^{SGS}}{\partial z^*} \tag{4}$$

where u_i ($i = 1, 2, 3$) are the velocity components in horizontal, transverse and vertical directions, respectively; (x^*, y^*, z^*, t^*) are the spatial and time coordinates in the physical domain; t is the time; p is the pressure; ρ_f is the water density; g_i ($i = 1, 2, 3$ or x, y, z) are the acceleration due to gravity; τ_{ij} and τ_{ij}^{SGS} ($i, j = 1, 2, 3$ or x, y, z) are shear stress and sub-grid scale (SGS) stress.

This model employs the σ coordinate in the vertical direction, as is shown below:

$$t = t^*, x = x^*, y = y^*, \sigma = \frac{z^* + h}{\eta + h} \tag{5}$$

where (x, y, σ, t) are the spatial and time coordinates in the σ coordinate system. η is the free surface displacement and h is the still water level. After the σ transformation, the spatially filtered Navier-Stokes equations can be transformed to:

$$\frac{\partial u_1}{\partial x} + \frac{\partial u_1}{\partial \sigma}\frac{\partial \sigma}{\partial x^*} + \frac{\partial u_2}{\partial y} + \frac{\partial u_2}{\partial \sigma}\frac{\partial \sigma}{\partial y^*} + \frac{\partial u_3}{\partial \sigma}\frac{\partial \sigma}{\partial z^*} = 0 \tag{6}$$

$$\begin{aligned}\frac{\partial u_1}{\partial t} + u_1\frac{\partial u_1}{\partial x} + u_2\frac{\partial u_1}{\partial y} + \omega\frac{\partial u_1}{\partial \sigma} = &-\frac{1}{\rho_f}\left(\frac{\partial p}{\partial x} + \frac{\partial p}{\partial \sigma}\frac{\partial \sigma}{\partial x^*}\right) + g_x + \frac{\partial \tau_{xx}}{\partial x} + \frac{\partial \tau_{xx}}{\partial \sigma}\frac{\partial \sigma}{\partial x^*} + \frac{\partial \tau_{xy}}{\partial y} + \frac{\partial \tau_{xy}}{\partial \sigma}\frac{\partial \sigma}{\partial y^*} + \frac{\partial \tau_{xz}}{\partial \sigma}\frac{\partial \sigma}{\partial z^*} - \\ &\frac{\partial \tau_{xx}^{SGS}}{\partial x} - \frac{\partial \tau_{xx}^{SGS}}{\partial \sigma}\frac{\partial \sigma}{\partial x^*} - \frac{\partial \tau_{xy}^{SGS}}{\partial y} - \frac{\partial \tau_{xy}^{SGS}}{\partial \sigma}\frac{\partial \sigma}{\partial y^*} - \frac{\partial \tau_{xz}^{SGS}}{\partial \sigma}\frac{\partial \sigma}{\partial z^*}\end{aligned} \tag{7}$$

$$\begin{aligned}\frac{\partial u_2}{\partial t} + u_1\frac{\partial u_2}{\partial x} + u_2\frac{\partial u_2}{\partial y} + \omega\frac{\partial u_2}{\partial \sigma} = &-\frac{1}{\rho_f}\left(\frac{\partial p}{\partial y} + \frac{\partial p}{\partial \sigma}\frac{\partial \sigma}{\partial y^*}\right) + g_y + \frac{\partial \tau_{yx}}{\partial x} + \frac{\partial \tau_{yx}}{\partial \sigma}\frac{\partial \sigma}{\partial x^*} + \frac{\partial \tau_{yy}}{\partial y} + \frac{\partial \tau_{yy}}{\partial \sigma}\frac{\partial \sigma}{\partial y^*} + \frac{\partial \tau_{yz}}{\partial \sigma}\frac{\partial \sigma}{\partial z^*} - \\ &\frac{\partial \tau_{yx}^{SGS}}{\partial x} - \frac{\partial \tau_{yx}^{SGS}}{\partial \sigma}\frac{\partial \sigma}{\partial x^*} - \frac{\partial \tau_{yy}^{SGS}}{\partial y} - \frac{\partial \tau_{yy}^{SGS}}{\partial \sigma}\frac{\partial \sigma}{\partial y^*} - \frac{\partial \tau_{yz}^{SGS}}{\partial \sigma}\frac{\partial \sigma}{\partial z^*}\end{aligned} \tag{8}$$

$$\begin{aligned}\frac{\partial u_3}{\partial t} + u_1\frac{\partial u_3}{\partial x} + u_2\frac{\partial u_3}{\partial y} + \omega\frac{\partial u_3}{\partial \sigma} = &-\frac{1}{\rho_f}\frac{\partial p}{\partial \sigma}\frac{\partial \sigma}{\partial z^*} + g_z + \frac{\partial \tau_{zx}}{\partial x} + \frac{\partial \tau_{zx}}{\partial \sigma}\frac{\partial \sigma}{\partial x^*} + \frac{\partial \tau_{zy}}{\partial y} + \frac{\partial \tau_{zy}}{\partial \sigma}\frac{\partial \sigma}{\partial y^*} + \frac{\partial \tau_{zz}}{\partial \sigma}\frac{\partial \sigma}{\partial z^*} - \\ &\frac{\partial \tau_{zx}^{SGS}}{\partial x} - \frac{\partial \tau_{zx}^{SGS}}{\partial \sigma}\frac{\partial \sigma}{\partial x^*} - \frac{\partial \tau_{zy}^{SGS}}{\partial y} - \frac{\partial \tau_{zy}^{SGS}}{\partial \sigma}\frac{\partial \sigma}{\partial y^*} - \frac{\partial \tau_{zz}^{SGS}}{\partial \sigma}\frac{\partial \sigma}{\partial z^*}\end{aligned} \tag{9}$$

where

$$\omega = \frac{\mathrm{D}\sigma}{\mathrm{D}t^*} = \frac{\partial \sigma}{\partial t^*} + u_1\frac{\partial \sigma}{\partial x^*} + u_2\frac{\partial \sigma}{\partial y^*} + u_3\frac{\partial \sigma}{\partial z^*} \tag{10}$$

As for the shear stress τ_{ij} and sub-grid shear stress τ_{ij}^{SGS} ($i, j = 1, 2, 3$), they can be calculated as:

$$\tau_{ij} = \nu\left(\frac{\partial u_i}{\partial x_j} + \frac{\partial u_i}{\partial \sigma}\frac{\partial \sigma}{\partial x_j^*} + \frac{\partial u_j}{\partial x_i} + \frac{\partial u_j}{\partial \sigma}\frac{\partial \sigma}{\partial x_i^*}\right) \tag{11}$$

$$\tau_{ij}^{SGS} = -2\nu_t S_{ij} = -\nu_t\left(\frac{\partial u_i}{\partial x_j} + \frac{\partial u_i}{\partial \sigma}\frac{\partial \sigma}{\partial x_j^*} + \frac{\partial u_j}{\partial x_i} + \frac{\partial u_j}{\partial \sigma}\frac{\partial \sigma}{\partial x_i^*}\right) \tag{12}$$

where ν is the kinematic viscosity; ν_t is the eddy viscosity, which can be obtained from the Smagorinsky model [53] as:

$$\nu_t = \left(C_s\Delta\right)^2\sqrt{2S_{ij}S_{ij}} \tag{13}$$

$$\Delta = \left(\Delta x_1 \Delta x_2 \Delta x_3\right)^{1/3} \tag{14}$$

where C_s is the Smagorinsky constant and should be calibrated and chosen based on the type of flow. In this study, the value is set to 0.2; Δ is a representative grid spacing and Δx_1, Δx_2, Δx_3 are the grid sizes in the coordinates of x^*, y^*, z^*, respectively.

2.2. Dispersed phase

The motion equation for a spherical particle within an unsteady and non-uniform fluid field is expressed as [24]:

$$\rho_p V_p \frac{\mathrm{d}\mathbf{u_p}}{\mathrm{d}t} = \mathbf{F_b} + \mathbf{F_d} + \mathbf{F_p} + \mathbf{F_a} + \mathbf{F_{Basset}} \tag{15}$$

where $\mathbf{F_b}$, $\mathbf{F_d}$, $\mathbf{F_p}$, $\mathbf{F_a}$, $\mathbf{F_{Basset}}$ are body force, drag force, fluid acceleration due to local pressure gradient, added mass force, Basset history force, respectively.

The body force $\mathbf{F_b}$ acting on a single particle is calculated by

$$\mathbf{F_b} = \left(\rho_f - \rho_p\right)V_p\mathbf{g} \tag{16}$$

where ρ_p is the particle density; V_p is the volume of particle and $\mathbf{g}$ is the gravitational acceleration.

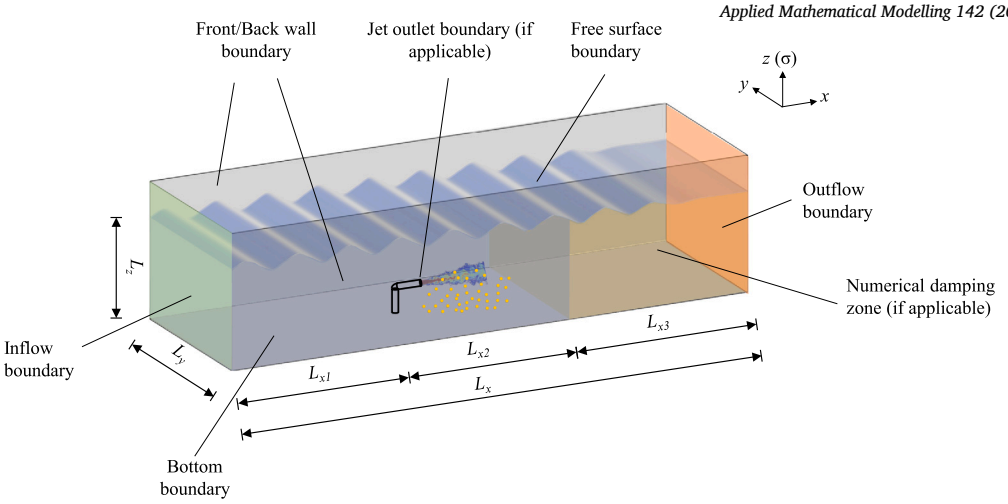

Fig. 1. Computational domain and boundary conditions.

The drag force $\mathbf{F_d}$ is expressed as follows:

$$\mathbf{F_d} = -\frac{1}{2}\rho_f C_d A_p \left|\mathbf{u_p} - \mathbf{u_f}\right| \left(\mathbf{u_p} - \mathbf{u_f}\right) \tag{17}$$

where A_p is the projected area of a particle; $\mathbf{u_p}$ is the particle velocity in three different directions; $\mathbf{u_f}$ is the fluid velocity in three different directions; C_d is the drag coefficient, it is related with particle Reynolds number Re_p as follows:

$$C_d = f(Re_p) = \begin{cases} \frac{24}{Re_p} & , Re_p < 0.4 \\ \frac{24}{Re_p}\left(1 + 0.15 Re_p^{0.687}\right) + \frac{0.42}{1+42500 Re_p^{-1.16}} & , 0.4 \le Re_p \le 1000 \\ 0.45 & , Re_p > 1000 \end{cases} \tag{18}$$

$$Re_p = \frac{\left|\mathbf{u_p} - \mathbf{u_f}\right| d}{\nu} \tag{19}$$

where d is the particle diameter.

The fluid acceleration due to local pressure gradient force $\mathbf{F_p}$ is formulated by:

$$\mathbf{F_p} = \rho_f V_p \left(\frac{\mathrm{d}\mathbf{u_f}}{\mathrm{d}t}\right)_f \tag{20}$$

The added mass force $\mathbf{F_a}$ follows:

$$\mathbf{F_a} = \rho_f C_M V_p \left[\frac{\mathrm{d}\mathbf{u_p}}{\mathrm{d}t} - \left(\frac{\mathrm{d}\mathbf{u_f}}{\mathrm{d}t}\right)_f\right] \tag{21}$$

where C_M is the added mass coefficient and equals 0.5.

The Basset history force $\mathbf{F_{Basset}}$ here follows:

$$\mathbf{F_{Basset}} = -\frac{3}{2} d^2 \sqrt{\pi \rho_f \mu} \int_0^t \frac{\frac{\mathrm{d}\mathbf{u_r}}{\mathrm{d}\tau}}{\sqrt{t-\tau}} d\tau \tag{22}$$

where μ is the dynamic viscosity of fluid and $\mathbf{u_r} = \mathbf{u_p} - \mathbf{u_f}$ is the relative velocity between particle and fluid.

2.3. Problem setup and boundary conditions

The setup of the computational domain is shown in Fig. 1. The dimensions of the domain are L_x in length, L_y in width and L_z in depth. For wave cases, a numerical damping zone with a length of L_{x3} is switched on to reduce wave reflection. For cases involving a jet, a jet outlet boundary is switched on. Additionally, the jet horizontal position is placed several meters upstream of the damping zone to maintain relatively stable flow conditions under wave conditions. A detailed description of the setup can be found in respective benchmark sections.

Six distinct boundary conditions, each corresponding to specific physical scenarios, are applied in this study. For the inflow boundary, both horizontal velocity $u_1(z,t)$, vertical velocity $u_3(z,t)$ and free surface displacement $\eta(t)$ are given by analytical expressions [54] for wave cases as:

$$\begin{aligned}
\eta(t) &= \frac{H}{2}\cos(\frac{\pi}{2}-\frac{2\pi}{T}t)+\frac{H^2k}{16}\frac{\cosh kh}{\sinh^3 kh}(2+\cosh 2kh)\cos 2(\frac{\pi}{2}-\frac{2\pi}{T}t), -h\le z\le 0\\
u_1(z,t) &= \frac{HgkT}{4\pi}\frac{\cosh k(h+z)}{\cosh kh}\cos(\frac{\pi}{2}-\frac{2\pi}{T}t)+\frac{3\pi H^2k}{8T}\frac{\cosh 2k(h+z)}{\sinh^4 kh}\cos 2(\frac{\pi}{2}-\frac{2\pi}{T}t), -h\le z\le 0\\
u_3(z,t) &= \frac{HgkT}{4\pi}\frac{\sinh k(h+z)}{\cosh kh}\sin(\frac{\pi}{2}-\frac{2\pi}{T}t)+\frac{3\pi H^2k}{8T}\frac{\sinh 2k(h+z)}{\sinh^4 kh}\sin 2(\frac{\pi}{2}-\frac{2\pi}{T}t), -h\le z\le 0
\end{aligned} \tag{23}$$

where H is the wave height from the mean water level, k is the wave number, T is the period of oscillation and h is the initial water depth. The pressure at the inflow boundary is derived based on the assumption of negligible vertical acceleration at the free surface and is expressed as follows [41]:

$$\frac{\partial p}{\partial x}+\frac{\partial p}{\partial \sigma}\frac{\partial \sigma}{\partial x^*}=-\rho_f g_z\frac{\partial \eta}{\partial x}, \frac{\partial p}{\partial y}+\frac{\partial p}{\partial \sigma}\frac{\partial \sigma}{\partial y^*}=-\rho_f g_z\frac{\partial \eta}{\partial y} \tag{24}$$

For the bottom boundary, velocity gradients at the first interior node are estimated using the free-slip boundary condition. These gradients are then utilized in advection calculations. Meanwhile, the log-law wall function is used to calculate wall shear stress for the diffusion step for the bottom boundary. The pressure gradient in the normal direction follows a hydrostatic assumption:

$$\frac{\partial p}{\partial \sigma}=\rho_f(\eta+h)g_z \tag{25}$$

This approach yields satisfactory results with relatively coarse meshes, as evidenced by Lin and Liu [55]. At the front/back wall boundary, conditions similar to those for the bottom boundary are applied. For the outflow boundary, a zero-gradient condition is imposed on the velocity in the normal direction, while the vertical pressure gradient follows the hydrostatic assumption.

For wave related cases, a numerical damping zone is applied at the outflow boundary to minimize wave reflection. This zone replicates experimental setups where breakwaters [56,57] or porous structures [58] are commonly placed near the end of the flume to dissipate waves. By employing this approach, surface waves are confined within the numerical channel, preventing artificial interactions with the boundary. The damping method utilized in this study can be expressed as [59]:

$$\phi_R=\phi+\Delta t\cdot\alpha\cdot\sigma\cdot\left(\frac{x-x_s}{x_e-x_s}\right)^2\cdot(\phi-\phi_0) \tag{26}$$

where ϕ is the variable to be solved, such as u_i and η. ϕ_R is the resulting variable after the numerical damping; The empirical parameter α is assigned a value of -1.0 in this study. The subscripts 's' and 'e' represent the start and end points of the damping zone in the x-direction, respectively.

Finally, at the moving free surface η, the pressure is assumed to be equal to the air pressure (i.e., equal to zero). And the kinematic boundary condition is set as:

$$\frac{\partial \eta}{\partial t}+u_1\frac{\partial \eta}{\partial x}+u_2\frac{\partial \eta}{\partial y}-u_3=0 \tag{27}$$

The jet velocity boundary is generated by the Synthetic-Eddy-Method (SEM) outlined by Jarrin et al. [60]. The instantaneous velocities at the jet outlet are divided into the sum of a time-averaged part and a fluctuating part. The time-averaged velocity at each node matches the experiment performed by Lu and Yuan [61]. The fluctuating part of the velocity field at each grid point is given as:

$$u_i{}'=\frac{1}{\sqrt{N}}\sum_{i=1}^{N}\varepsilon_i f_\sigma(x_i-x)f_\sigma(y_i) \tag{28}$$

where

$$f_\sigma\left(\bar{x}-\bar{x}^k(t)\right)=\sqrt{\frac{V_B}{\sigma_x\sigma_y\sigma_z}}\cdot f\left(\frac{x-x^k(t)}{\sigma_x}\right)\cdot f\left(\frac{y-y^k(t)}{\sigma_y}\right)\cdot f\left(\frac{z-z^k(t)}{\sigma_z}\right) \tag{29}$$

The triangular function is written as

$$f(\zeta)=\begin{cases}\sqrt{1.5}(1-|\zeta|) & |\zeta|\le 1\\ 0 & |\zeta|>1\end{cases} \tag{30}$$

Detailed description on the method can be found in Jarrin et al. [60]. In this study, the fluctuation velocity and Reynolds stress distribution align with the DNS results conducted by Wu and Moin [62].

3. Numerical methods

3.1. Fluid phase

3.1.1. Numerical schemes for Navier-Stokes equations

An operator splitting technique [63,64] is utilized for the numerical solution of the governing equations. Within each time interval, the momentum equations are segmented into three separate steps, namely advection, diffusion, and pressure propagation [41]. For brevity, in this part, only governing equations in the horizontal direction will be presented below, equations in other directions can be solved in a similar way.

The finite difference form for the advection step is shown as:

$$\frac{(u_1)_{i,j,k}^{n+1/3}-(u_1)_{i,j,k}^{n}}{\Delta t}=-\left(u_1\frac{\partial u_1}{\partial x}+u_2\frac{\partial u_1}{\partial y}+\omega\frac{\partial u_1}{\partial \sigma}\right)_{i,j,k}^{n} \tag{31}$$

Equation (31) can be further split into following three sub-steps:

$$\begin{aligned}
\frac{(u_1)_{i,j,k}^{n+1/9}-(u_1)_{i,j,k}^{n}}{\Delta t}&=-\left(u_1\frac{\partial u_1}{\partial x}\right)_{i,j,k}^{n}\\
\frac{(u_1)_{i,j,k}^{n+2/9}-(u_1)_{i,j,k}^{n+1/9}}{\Delta t}&=-\left(u_2\frac{\partial u_1}{\partial y}\right)_{i,j,k}^{n+1/9}\\
\frac{(u_1)_{i,j,k}^{n+3/9}-(u_1)_{i,j,k}^{n+2/9}}{\Delta t}&=-\left(\omega\frac{\partial u_1}{\partial \sigma}\right)_{i,j,k}^{n+2/9}
\end{aligned} \tag{32}$$

To solve these above equations, the quadratic backward characteristic method [65] and the Lax-Wendroff method are employed at the same time. Final numerical results are calculated by using the average value on the above two methods to ensure stability and accuracy, which can be written as:

$$(u_1)_{i,j,k}^{n+1/9}=\frac{\left[(u_1)_{i,j,k}^{n+1/9}\right]_{QC}+\left[(u_1)_{i,j,k}^{n+1/9}\right]_{LW}}{2} \tag{33}$$

where

$$\begin{aligned}
\left[(u_1)_{i,j,k}^{n+1/9}\right]_{QC}=&\frac{\left(\Delta x_{i-1}-\Delta x_a\right)\left(-\Delta x_a\right)}{\Delta x_{i-2}\left(\Delta x_{i-2}+\Delta x_{i-1}\right)}(u_1)_{i-2,j,k}^{n}+\frac{\left(\Delta x_{i-2}+\Delta x_{i-1}-\Delta x_a\right)\left(-\Delta x_a\right)}{\left(\Delta x_{i-2}\right)\left(-\Delta x_{i-1}\right)}(u_1)_{i-1,j,k}^{n}\\
&+\frac{\left(\Delta x_{i-2}+\Delta x_{i-1}-\Delta x_a\right)\left(\Delta x_{i-1}-\Delta x_a\right)}{\left(\Delta x_{i-2}+\Delta x_{i-1}\right)\Delta x_{i-1}}(u_1)_{i,j,k}^{n}
\end{aligned} \tag{34}$$

$$\begin{aligned}
\left[(u_1)_{i,j,k}^{n+1/9}\right]_{LW}=&\frac{\Delta x_a\left(\Delta x_i+\Delta x_a\right)}{\Delta x_{i-1}\left(\Delta x_{i-1}+\Delta x_i\right)}(u_1)_{i-1,j,k}^{n}+\frac{\left(\Delta x_{i-1}-\Delta x_a\right)\left(-\Delta x_i-\Delta x_a\right)}{\Delta x_{i-1}\left(-\Delta x_i\right)}(u_1)_{i,j,k}^{n}\\
&+\frac{\left(\Delta x_{i-1}-\Delta x_a\right)\left(-\Delta x_a\right)}{\left(\Delta x_{i-1}+\Delta x_i\right)\Delta x_i}(u_1)_{i+1,j,k}^{n}
\end{aligned} \tag{35}$$

In the above equations, the Δx_a is the advection distance and is defined as $\Delta x_a=(u_1)_{i,j,k}^{n}\Delta t$.

In the diffusion step, the equation to be solved is as follows:

$$\begin{aligned}
\frac{(u_1)_{i,j,k}^{n+2/3}-(u_1)_{i,j,k}^{n+1/3}}{\Delta t}=&\left(\frac{\partial \tau_{xx}}{\partial x}+\frac{\partial \tau_{xx}}{\partial \sigma}\frac{\partial \sigma}{\partial x^*}+\frac{\partial \tau_{xy}}{\partial y}+\frac{\partial \tau_{xy}}{\partial \sigma}\frac{\partial \sigma}{\partial y^*}+\frac{\partial \tau_{xz}}{\partial \sigma}\frac{\partial \sigma}{\partial z^*}-\frac{\partial \tau_{xx}^{SGS}}{\partial x}-\right.\\
&\left.\frac{\partial \tau_{xx}^{SGS}}{\partial \sigma}\frac{\partial \sigma}{\partial x^*}-\frac{\partial \tau_{xy}^{SGS}}{\partial y}-\frac{\partial \tau_{xy}^{SGS}}{\partial \sigma}\frac{\partial \sigma}{\partial y^*}-\frac{\partial \tau_{xz}^{SGS}}{\partial \sigma}\frac{\partial \sigma}{\partial z^*}\right)_{i,j,k}^{n+1/3}
\end{aligned} \tag{36}$$

The stress term can be calculated according to Equation (11) and Equation (12). The central difference is used to discretize all partial differentiation terms in the above equation as:

$$\left(\frac{\partial \tau_{xx}}{\partial x}\right)_{i,j,k}^{n+1/3}=\frac{\left(\tau_{xx}\right)_{i+1/2,j,k}^{n+1/3}-\left(\tau_{xx}\right)_{i-1/2,j,k}^{n+1/3}}{\left(\Delta x_{i-1}+\Delta x_i\right)/2} \tag{37}$$

where

$$\left(\tau_{xx}\right)_{i+1/2,j,k}^{n+1/3}=\left(\nu+\nu_t\right)\left(\frac{(u_1)_{i+1,j,k}^{n+1/3}-(u_1)_{i,j,k}^{n+1/3}}{\Delta x_i}+\frac{(u_1)_{i+1/2,j,k+1}^{n+1/3}-(u_1)_{i+1/2,j,k-1}^{n+1/3}}{\Delta\sigma_{k-1}+\Delta\sigma_k}\left(\frac{\partial\sigma}{\partial x^*}\right)_{i+1/2,j,k}^{n+1/3}\right) \tag{38}$$

$$\left(\tau_{xx}\right)_{i-1/2,j,k}^{n+1/3}=\left(\nu+\nu_t\right)\left(\frac{(u_1)_{i,j,k}^{n+1/3}-(u_1)_{i-1,j,k}^{n+1/3}}{\Delta x_{i-1}}+\frac{(u_1)_{i-1/2,j,k+1}^{n+1/3}-(u_1)_{i-1/2,j,k-1}^{n+1/3}}{\Delta\sigma_{k-1}+\Delta\sigma_k}\left(\frac{\partial\sigma}{\partial x^*}\right)_{i-1/2,j,k}^{n+1/3}\right) \tag{39}$$

In the above equations, $(u_1)_{i+1/2,j,k+1}^{n+1/3}$ means the velocity between nodes and can be obtained by the linear interpolation.
In the pressure propagation step, the following equation is to be solved:

$$\frac{(u_1)_{i,j,k}^{n+1}-(u_1)_{i,j,k}^{n+2/3}}{\Delta t}=-\frac{1}{\rho_f}\left(\frac{\partial p}{\partial x}+\frac{\partial p}{\partial\sigma}\frac{\partial\sigma}{\partial x^*}\right)_{i,j,k}^{n+1}+g_x \tag{40}$$

The central difference scheme in space is used to discretize the above two equations. To satisfy the continuity requirement, the resultant equation is incorporated into the continuity equation, leading to the derivation of the modified Poisson equation as follows:

$$\begin{aligned}&\left\{\frac{\partial^2 p}{\partial x^2}+\frac{\partial^2 p}{\partial y^2}+\left[\left(\frac{\partial\sigma}{\partial x^*}\right)^2+\left(\frac{\partial\sigma}{\partial y^*}\right)^2+\left(\frac{\partial\sigma}{\partial z^*}\right)^2\right]\frac{\partial^2 p}{\partial\sigma^2}+2\left(\frac{\partial\sigma}{\partial x^*}\frac{\partial^2 p}{\partial x\partial\sigma}+\frac{\partial\sigma}{\partial y^*}\frac{\partial^2 p}{\partial y\partial\sigma}\right)+\left(\frac{\partial^2\sigma}{\partial x^*\partial x}+\frac{\partial^2\sigma}{\partial y^*\partial y}\right)\frac{\partial p}{\partial\sigma}\right\}_{i,j,k}^{n+1}\\&=\frac{\rho_f}{\Delta t}\left(\frac{\partial u_1}{\partial x}+\frac{\partial u_1}{\partial\sigma}\frac{\partial\sigma}{\partial x^*}+\frac{\partial u_2}{\partial y}+\frac{\partial u_2}{\partial\sigma}\frac{\partial\sigma}{\partial y^*}+\frac{\partial u_3}{\partial\sigma}\frac{\partial\sigma}{\partial z^*}\right)_{i,j,k}^{n+2/3}\end{aligned} \tag{41}$$

The CGSTAB method is used to solve the pressure Equation (41) discretized using central differences [66].

3.1.2. Lagrangian-Eulerian method for tracking free surface

In order to get the surface elevation, the Lagrange–Euler method [66] is adopted in this study. Assume we have a particle which is at the free surface, the location of this particle at t_{n+1} is marked as $\left(x_{t_{n+1}},y_{t_{n+1}}\right)$ and we can also mark the corresponding particle position at t_n as $\left(x_{t_n},y_{t_n}\right)$. By the Lagrange displacement equation and Taylor expansion, we can get the following equations:

$$\begin{aligned}x_{t_{n+1}}-x_{t_n}&=\int_{t_n}^{t_{n+1}}u_1\left(x(t),y(t),t\right)dt=u_1\left(x\left(t_\theta\right),y\left(t_\theta\right),t_\theta\right)\Delta t\\&=\left\{u_{1\,i,j}^{n+1}-\theta\left(\frac{\partial u_1}{\partial x}\right)_{i,j}^{n+1}\left(x_{t_{n+1}}-x_{t_n}\right)-\theta\left(\frac{\partial u_1}{\partial y}\right)_{i,j}^{n+1}\left(y_{t_{n+1}}-y_{t_n}\right)-\theta\left(\frac{\partial u_1}{\partial t}\right)_{i,j}^{n+1}\Delta t\right\}\Delta t\end{aligned} \tag{42}$$

$$\begin{aligned}y_{t_{n+1}}-y_{t_n}&=\int_{t_n}^{t_{n+1}}u_2\left(x(t),y(t),t\right)dt=u_2\left(x\left(t_\theta\right),y\left(t_\theta\right),t_\theta\right)\Delta t\\&=\left\{u_{2\,i,j}^{n+1}-\theta\left(\frac{\partial u_2}{\partial x}\right)_{i,j}^{n+1}\left(x_{t_{n+1}}-x_{t_n}\right)-\theta\left(\frac{\partial u_2}{\partial y}\right)_{i,j}^{n+1}\left(y_{t_{n+1}}-y_{t_n}\right)-\theta\left(\frac{\partial u_2}{\partial t}\right)_{i,j}^{n+1}\Delta t\right\}\Delta t\end{aligned} \tag{43}$$

The central difference method for spatial derivatives and the forward difference method for temporal derivatives are used to determine the variables (x_{t_n}, y_{t_n}) by solving Equation (42) and Equation (43). Given the particle's location within element (i, j) at time t_n, the initial surface elevation $\eta_{x,y}^n$ is interpolated from the grid node values within the element. Subsequently, the Lagrange displacement equation is applied to update the surface elevation at the subsequent time step $n+1$.

$$\eta_{i,j}^{n+1}=\eta_{i,j}^n+\left\{u_{3\,i,j}^{n+1}-\theta\left(\frac{\partial u_3}{\partial x}\right)_{i,j}^{n+1}\left(x_{t_{n+1}}-x_{t_n}\right)-\theta\left(\frac{\partial u_3}{\partial y}\right)_{i,j}^{n+1}\left(y_{t_{n+1}}-y_{t_n}\right)-\theta\left(\frac{\partial u_3}{\partial t}\right)_{i,j}^{n+1}\Delta t\right\}\Delta t \tag{44}$$

3.1.3. Stability criteria

To ensure the stability and computational efficiency of this model, two criteria must be met. The first criterion is related to the Courant-Friedrichs-Lewy (CFL) condition, which is expressed as:

$$\Delta t\le\beta\cdot\max\left(\frac{\Delta x_i}{(u_i)_{\max}}\right) \tag{45}$$

Here, $i=1,2,3$ refers to the spatial dimensions (horizontal, transverse, and vertical), with Δx_i representing the grid sizes and $(u_i)_{\max}$ denoting the maximum particle velocity in each respective direction. Although the theoretical upper limit for β is 1.0, in practice, it is generally assigned a more conservative value below 0.2 to maintain both stability and computational accuracy. In this model, the value is set to 0.1.

Another criterion applies to the diffusion term, which requires the following condition to be met:

$$\Delta t \leq \gamma \cdot \frac{(\Delta x_i)^2}{\nu} \tag{46}$$

where γ is typically assigned a value of 0.2. However, in most practical simulations, the time step is primarily constrained by the more restrictive CFL condition in Equation (45), as it imposes a tighter limit on the time step size due to the higher velocities encountered in the advection process.

3.2. Dispersed phase

When it comes to the dispersed phase, one main difficulty lies in how to get numerical solution of the Basset force, as the integrand is ill-behaved and would become an infinity when $\tau \longrightarrow t$. To address this issue, the integral is divided into a series of small integrals, each calculated over a brief time step Δt. Assuming that the variation in relative velocity can be determined using the central difference method and that acceleration remains constant during Δt, the Basset integral can be computed as the cumulative total of these smaller integrals [67]. Hence, $\frac{\mathrm{d}\mathbf{u_r}}{\mathrm{d}t}$ is evaluated at the middle of the time step.

$$\begin{aligned}
\mathbf{B} =& \int_0^{t+\Delta t} \frac{\frac{\mathrm{d}\mathbf{u_r}}{\mathrm{d}\tau}}{\sqrt{t+\Delta t-\tau}}\mathrm{d}\tau \\
=& \int_0^{\Delta t} \frac{\frac{\mathrm{d}\mathbf{u_r^0}}{\mathrm{d}\tau}}{\sqrt{t+\Delta t-\tau}}\mathrm{d}\tau + \int_{\Delta t}^{2\Delta t} \frac{\frac{\mathrm{d}\mathbf{u_r^{\Delta t}}}{\mathrm{d}\tau}}{\sqrt{t+\Delta t-\tau}}\mathrm{d}\tau + \ldots + \int_{M\Delta t}^{M\Delta t+\Delta t} \frac{\frac{\mathrm{d}\mathbf{u_r^{M\Delta t}}}{\mathrm{d}\tau}}{\sqrt{t+\Delta t-\tau}}\mathrm{d}\tau \\
=& \frac{\mathrm{d}\mathbf{u_r^0}}{\mathrm{d}\tau}\int_0^{\Delta t} \frac{1}{\sqrt{t+\Delta t-\tau}}\mathrm{d}\tau + \frac{\mathrm{d}\mathbf{u_r^{\Delta t}}}{\mathrm{d}\tau}\int_{\Delta t}^{2\Delta t} \frac{1}{\sqrt{t+\Delta t-\tau}}\mathrm{d}\tau + \ldots + \frac{\mathrm{d}(\mathbf{u_p}-\mathbf{u_f})}{\mathrm{d}\tau}\int_{M\Delta t}^{M\Delta t+\Delta t} \frac{1}{\sqrt{t+\Delta t-\tau}}\mathrm{d}\tau \\
=& \frac{\mathbf{u_{r,1}}-\mathbf{u_{r,0}}}{\Delta t}\cdot 2(\sqrt{M\Delta t+\Delta t}-\sqrt{M\Delta t-\Delta t+\Delta t}) + \ldots + \frac{\mathbf{u_{r,M}}-\mathbf{u_{r,M-1}}}{\Delta t}\cdot \\
& 2(\sqrt{M\Delta t-(M-1)\Delta t+\Delta t}-\sqrt{M\Delta t-M\Delta t+\Delta t}) + 2\sqrt{\Delta t}\frac{d(\mathbf{u_p}-\mathbf{u_f})}{\mathrm{d}t} \\
=& \frac{2}{\sqrt{\Delta t}}\sum_{n=0}^{M-1}\left[(\mathbf{u_{r,n+1}}-\mathbf{u_{r,n}})\left(\sqrt{M-n+1}-\sqrt{M-n-1+1}\right)\right] + 2\sqrt{\Delta t}\frac{\mathrm{d}(\mathbf{u_p}-\mathbf{u_f})}{\mathrm{d}t} \\
=& \mathbf{B_0^t} + 2\sqrt{\Delta t}\frac{\mathrm{d}(\mathbf{u_p}-\mathbf{u_f})}{\mathrm{d}t}
\end{aligned} \tag{47}$$

where $\mathbf{B_0^t}$ is the Basset integral between $\tau = 0$ to t.

At $\tau = t$, the simplified version of Equation (15) can be written as

$$\frac{\mathrm{d}\mathbf{u_p}}{\mathrm{d}t} = \frac{\left[(1-s)g + (1+C_M)(\frac{\mathrm{d}\mathbf{u_f}}{\mathrm{d}t})_f - \frac{3C_D}{4d}\left|\mathbf{u_p}-\mathbf{u_f}\right|(\mathbf{u_p}-\mathbf{u_f}) - \frac{9}{d}\sqrt{\frac{\nu}{\pi}}\mathbf{B_0^t}\right]}{(s+C_M)} = \mathbf{F} \tag{48}$$

While when $\tau = t + \Delta t$, after applying the Equation (47), the governing equation can be written as

$$\frac{\mathrm{d}\mathbf{u_p}}{\mathrm{d}t} = \frac{\left[(1-s)g + (1+C_M+\frac{18}{d}\sqrt{\frac{\nu}{\pi}\Delta t})(\frac{\mathrm{d}\mathbf{u_f}}{\mathrm{d}t})_f - \frac{3C_D}{4d}\left|\mathbf{u_p}-\mathbf{u_f}\right|(\mathbf{u_p}-\mathbf{u_f}) - \frac{9}{d}\sqrt{\frac{\nu}{\pi}}\mathbf{B_0^t}\right]}{(s+C_M+\frac{18}{d}\sqrt{\frac{\nu}{\pi}\Delta t})} \tag{49}$$

At the Nth time step, the particle position $\mathbf{x_{p,N}}$, particle velocity $\mathbf{u_{p,N}}$, and flow velocity $\mathbf{u_{f,N}}$ are known. Initially, a preliminary estimate for the particle velocity $\mathbf{u_{p,N+1}} = \mathbf{u_{p,N}} + \Delta t \times \mathbf{F}(\mathbf{u_{p,N}}, \mathbf{x_{p,N}})$ is made at $\tau = t + \Delta t$, enabling the calculation of the corresponding particle position $\mathbf{x_{p,N}}$. Subsequently, a second-order implicit iteration method is employed to determine the particle's velocity and position at the $(N+1)$th time step. This iterative process continues until the relative deviation between two successive iterations is less than 0.1%. Ultimately, the final particle velocity and position are obtained. It is noteworthy that this numerical method is applicable beyond situations where the Basset force is considered. In scenarios where the Basset force is excluded, the term $\mathbf{B_0^t}$ can be disregarded, and the equations in Equation (48) can be further simplified. The detailed numerical scheme for solving the governing equation of the dispersed phase is outlined in Algorithm 1.

3.3. Solution procedure

In order to make the solution procedure of the model a more direct and easier to understand, a flow chart is presented in Fig. 2.

1. Calculate $u_i^{n+1/3}$ $(i = 1, 2, 3)$ at advection step from Equations (31)-(35).

Algorithm 1 Numerical method for dispersed phase.

$\mathbf{u}_{p,N+1}{}^{(0)} \leftarrow \mathbf{u}_{p,N} + \Delta t * \mathbf{F}(\mathbf{u}_{p,N}, \mathbf{x}_{p,N})$, $\mathbf{x}_{p,N+1}{}^{(0)} \leftarrow \mathbf{x}_{p,N} + \Delta t * \mathbf{u}_{p,N+1}{}^{(0)}$
while $\left[\mathbf{u}_{p,N+1}{}^{(k+1)} - \mathbf{u}_{p,N+1}{}^{(k)}\right] / \mathbf{u}_{p,N+1}{}^{(k)} \geq 10^{-3}$ **do**
  $\mathbf{u}_{p,N+1}{}^{(k+1)} \leftarrow \mathbf{u}_{p,N} + \frac{\Delta t}{2} * \left[\mathbf{F}\left(\mathbf{u}_{p,N}, \mathbf{x}_{p,N}\right) + \mathbf{F}\left(\mathbf{u}_{p,N+1}{}^{(k)}, \mathbf{x}_{p,N+1}{}^{(k)}\right)\right]$; $\mathbf{x}_{p,N+1}{}^{(k+1)} \leftarrow \mathbf{x}_{p,N} + \mathbf{u}_{p,N+1}{}^{(k+1)} * \Delta t$, $k = 0, 1, 2, \ldots$
end while
$\mathbf{u}_{p,N+1} \leftarrow \mathbf{u}_{p,N+1}{}^{(k+1)}$, $\mathbf{x}_{p,N+1} \leftarrow \mathbf{x}_{p,N+1}{}^{(k+1)}$

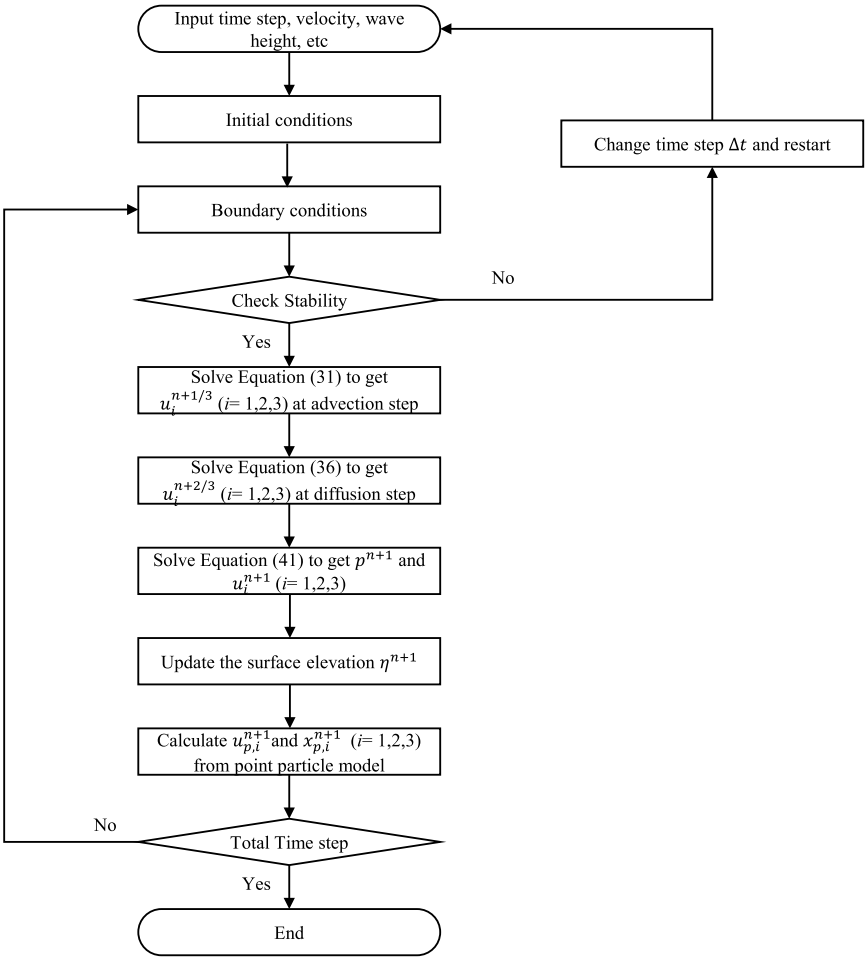

Fig. 2. Solution procedure of the model.

2. Solve Equations (36) to obtain $u_i^{n+2/3}$ $(i = 1, 2, 3)$ in the diffusion step.
3. Use the Conjugate Gradient Squared (CGSTAB) method to solve Equation (41) for the pressure field p^{n+1} and velocity u_i^{n+1}.
4. Calculate the free surface displacement η^{n+1} using Equation (44).
5. Get the particle positions and velocities from Equation (49), based on the flow velocities derived in Steps 1-3.

4. Results and discussion

4.1. Benchmark: non-hydrostatic wave flume

4.1.1. Regular waves

A regular progressive wave is generated in the non-hydrostatic wave flume, as depicted in Fig. 1. The dimensions of the flume are $L_x = 15$ m in length, $L_y = 0.5$ m in width, and $L_z = 0.5$ m in depth. The damping zone has a length of $L_{x3} = 5$ m and is positioned at the end of the flume to dissipate wave energy. The amplitude of the regular wave is 0.02 m and the wave period is 1 s.

Eight different grid systems, as detailed in Table 1, are performed to check the spatial convergence of the model. Grid1 to Grid4 focus on spatial convergence in the horizontal direction, while Grid2 and Grid5 to Grid8 are employed for the convergence in

Table 1
Grid systems of spatial convergence study on regular waves.

Grid	Grid points	min Δx	min $\Delta\sigma$
Grid-1	151x11x101	0.1 m	0.01
Grid-2	301x11x101	0.05 m	0.01
Grid-3	601x11x101	0.025 m	0.01
Grid-4	1201x11x101	0.0125 m	0.01
Grid-5	301x11x51	0.05 m	0.02
Grid-6	301x11x41	0.05 m	0.025
Grid-7	301x11x21	0.05 m	0.05
Grid-8	301x11x11	0.05 m	0.1

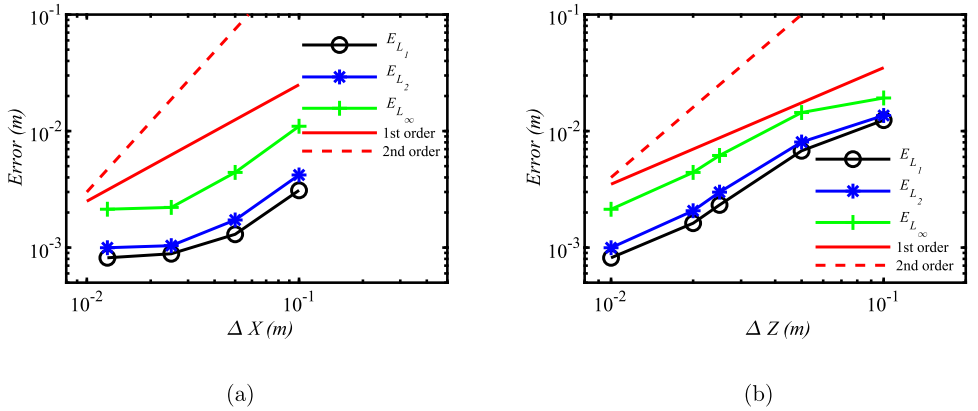

Fig. 3. Spatial convergence study of regular waves along the whole flume at $t = 25$ s: (a) horizontal direction; (b) vertical direction.

the vertical direction. For the transverse direction, the inflow condition of the water level along this direction is the same and as discussed in Section 2.3, a zero-gradient condition is applied to the wall's normal direction. The discretization in the y-direction does not influence changes in the water level η. Hence, fixed grids are set in the transverse direction for all the cases. The grids are uniformly distributed in both horizontal and vertical directions. The normalized L_1 error E_{L_1}, L_2 error E_{L_2}, and maximum error E_{L_∞} were used in this test, which were calculated as follows:

$$E_{L_1} = \frac{\sum \left|\eta_{numerical} - \eta_{analytical}\right|}{n} \tag{50}$$

$$E_{L_2} = \sqrt{\frac{\sum(\eta_{numerical} - \eta_{analytical})^2}{n}} \tag{51}$$

$$E_{L_\infty} = max\left|\eta_{numerical} - \eta_{analytical}\right| \tag{52}$$

In Grid systems 1–4, the water depth is discretized using 100 uniform grids, while the horizontal direction is discretized with varying uniform grids. As shown in Fig. 3(a), the convergence order in the horizontal direction approaches first-order accuracy. Similarly, Fig. 3(b) demonstrates that the convergence order in the vertical direction is also close to the first order. Finally, Grid-3 was selected for the simulation in this case.

Fig. 4 shows the spatial profiles of water level throughout the entire flume at $t = 25$ s, as well as the temporal profile of water level at $x = 6$ m. Evidently, the numerical results match well with analytical solutions. Additionally, Fig. 4(a) demonstrates that wave reflection is negligible within the effective zone (0 m-10 m), which proves that wave energy was dissipated effectively in the damping zone (10 m-15 m). Fig. 5 shows the relative volume of water over time for regular waves. It can be seen that the volume of water preserves well and stabilizes after 30 seconds, which confirms the validity of the model.

Fig. 6 shows the maximum horizontal velocity distribution and maximum vertical velocity distribution along water depth in one wave period and their comparison with analytical solutions at $x = 6$ m. The comparison of horizontal and vertical velocity distributions with analytical results reveals negligible differences, indicating the flow field is well simulated. It is worth mentioning that a slight difference in the horizontal velocity can be seen in Fig. 6 close to the bottom, and this can be attributed to the wave boundary layer which exists at a very narrow range close to the bottom. Due to the existence of the boundary layer, the real velocity distribution would deviate from the analytical solution close to the bottom. In addition, the velocity should equal zero at the bottom, which is consistent with our numerical results. In summary, the numerical model successfully replicates both the water surface changes and the velocity distribution of regular waves.

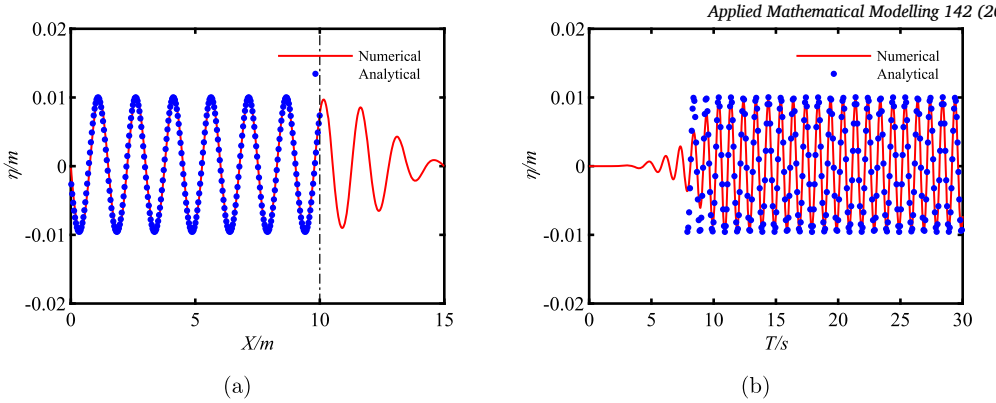

Fig. 4. Free surface verification for the regular waves: (a) Spatial distribution of water level along the whole flume at $t = 25$ s; (b) Temporal distribution of water level at $x = 6$ m.

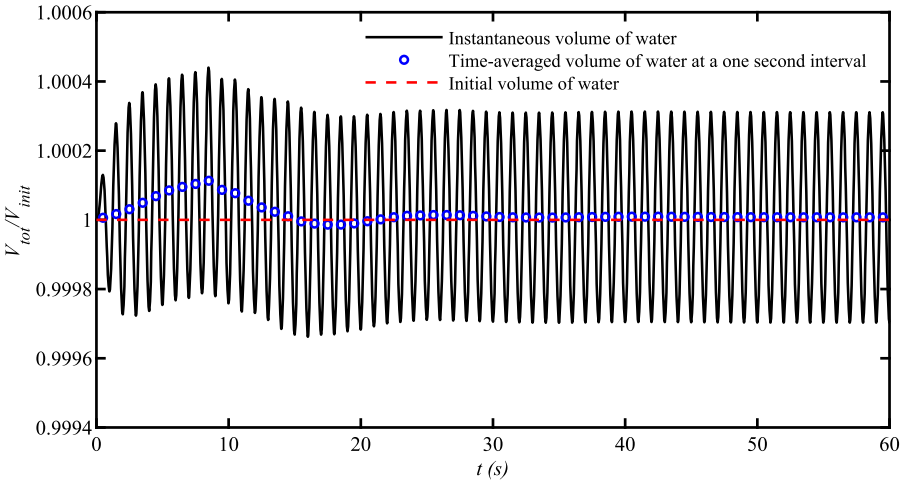

Fig. 5. Relative volume of water over time for the regular waves.

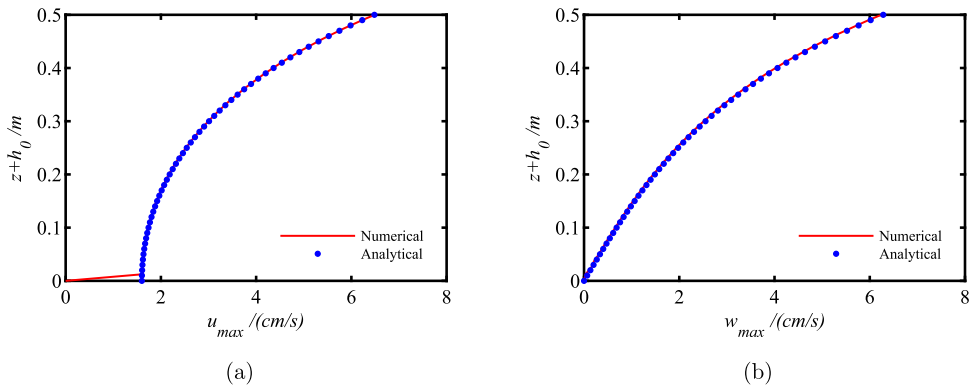

Fig. 6. Verification of the velocity distribution of a regular wave: (a) the horizontal velocity distribution along water depth in wave peak phase; (b) the vertical velocity distribution along water depth in up-zero crossing phase.

4.1.2. Wave-structure interaction

When a regular wave encounters a submerged bar, it frequently experiences significant changes in the waveform, resulting in noteworthy nonlinear energy interactions among various wave modes [41]. The simulation of such case is imperative, as it serves as a foundational test case for numerical tanks and can yield critical insights into the dynamics of wave interactions with submerged structures.

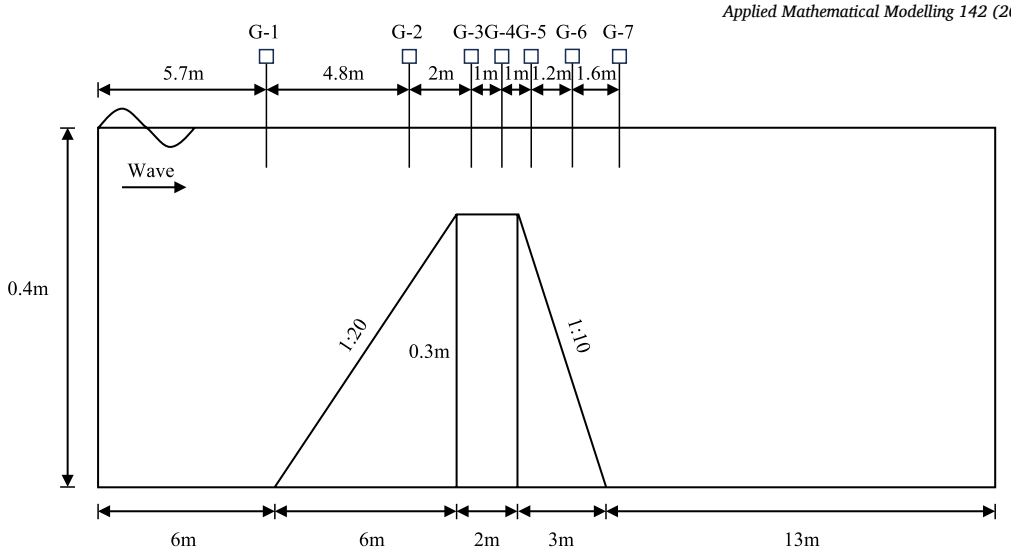

Fig. 7. Sketch of the geometry for a regular wave passing the submerged bar. PS: G stands for wave gauges.

Table 2
Mesh convergence study on wave-structure interaction.

Grid	Grid points	min Δx	min Δy	min $\Delta\sigma$
Grid-1	1201x9x47	0.025 m	0.05 m	0.011
Grid-2	2401x5x47	0.0125 m	0.10 m	0.011
Grid-3	2401x9x24	0.0125 m	0.05 m	0.022
Grid-4	2401x9x47	0.0125 m	0.05 m	0.011
Grid-5	2401x9x93	0.0125 m	0.05 m	0.0055
Grid-6	2401x17x47	0.0125 m	0.025 m	0.011
Grid-7	4801x9x47	0.00625 m	0.05 m	0.011

Our numerical simulations are based on experiments conducted by Beji and Battjes [68]. The geometry of our numerical computations is depicted in Fig. 7. The length of the flume is 30 m, the width is 0.5 m and the water depth is 0.4 m. A regular wave with a wave height of 0.02 m and a period of 2 s is generated from the inflow boundary and the damping zone L_{x3} is set as 10 m to dissipate the wave energy. Seven wave gauges are positioned at various locations within the flume. To ensure grid convergence, seven different grid configurations are employed in the model (as shown in Table 2), with a time step of $\Delta t = 0.005$ s. The simulations were carried out on a desktop computer with an AMD Ryzen(TM) 5 5600X CPU and 16 GB internal memory. The base frequency of this CPU is 3.7 GHz. The total CPU time per time step required for the present model was about 1.8 s.

The comparisons between our numerical findings and the gauge data for free surface elevation at six designated locations are depicted in Fig. 8. The results from seven different grid systems are also presented in the figure. For most grid systems, the numerical simulation results match well with the experimental data, except for Grid-3, where a distinct phase lag is observed. This discrepancy can be attributed to the relatively low grid resolution at the free surface. Ultimately, Grid-4 is selected for the simulation in this case. It was found that at wave gauge 2 ($x = 10.5$ m), the wave retains its sinusoidal feature, displaying strong concurrence between the numerical results and experimental data. Moving from $x = 10.5$ m to $x = 12.5$ m, we observe the wave deformation as it climbs the slope. From wave gauge 4 ($x = 13.5$ m) to 7 ($x = 17.5$ m), where the wave surmounts the breakwater, exhibit the emergence of secondary wave growth.

Fig. 9 shows the top and side view plots of the 3D free surface elevation at a representative time. The red, yellow, black, and blue rectangle represents the upslope part, horizontal part, downslope part, and damping zone, respectively. It can be seen that the wavelength gradually decreases while the wave height increases during the wave shoaling process. On the contrary, a decrease in wave height is observed when the wave moves downhill, and more small waves can be seen. It can be attributed to the dissipation in wave energy which in return lead to the generation of higher-order secondary waves. In summary, the numerical model accurately captures this progression, although minor disparities in the variation of wave height exist between the numerical results and experimental data. These distinctions may arise from numerical dissipation and the σ transformation, stemming from the abrupt change in water depth.

4.2. Benchmark: point particle

To validate the point-particle model, the accelerated process of a spherical particle settling in a stationary fluid is simulated. When the particle Reynolds number Re_p is relatively small (i.e., $Re_p < 0.4$), the analytical solution of the acceleration process can be

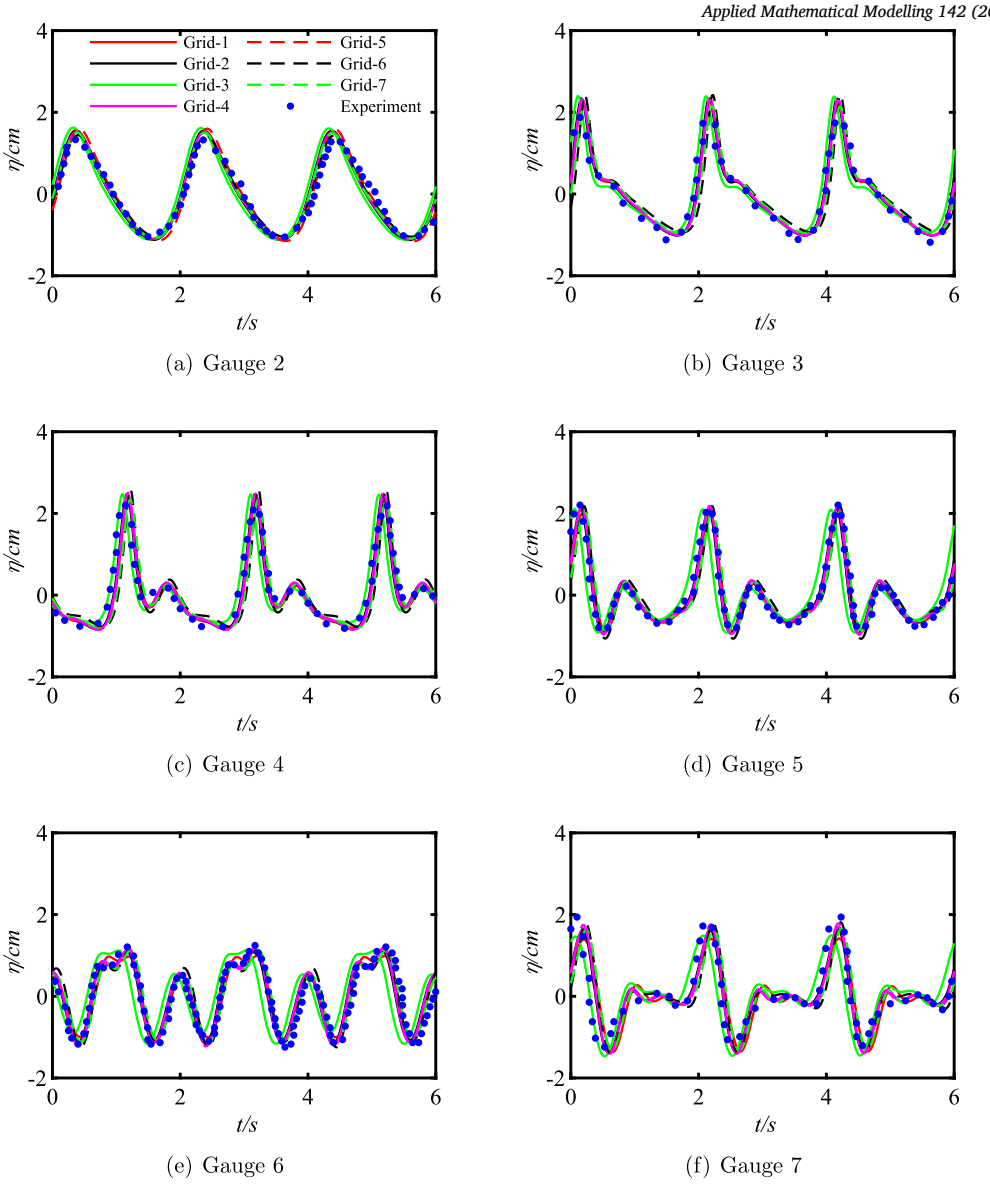

Fig. 8. Comparison of the wave elevation between numerical results and experiment results at six different gauge points.

derived from linear (Stokes) drag law. By neglecting the Basset history term and assuming an initial velocity of zero, we can derive the temporal evolution of particle velocity as follows:

$$w_p(t) = \frac{(s-1)gd^2}{18\nu}\left(1 - e^{-\frac{18\nu t}{d^2(s+C_M)}}\right) \tag{53}$$

When the Basset force is considered, the analytical solution can be found in Brush et al. [69] in a closed-form solution:

$$\begin{aligned} w_p(t) = \frac{(s-1)gd^2}{18\nu}\Bigg\{1 + \frac{\sqrt{c^2+h^2}}{h}\exp\left(-h^2 t\right)\Bigg[\exp\left(c^2 t\right)\sin\left(2ch t - \alpha\right)\operatorname{erfc}\left(c\sqrt{t}\right) \\ - 2\sqrt{\frac{t}{\pi}}\int_0^h \exp\left(y^2 t\right)\cos\left[2c\left(h-y\right)t - \alpha\right]dy\Bigg]\Bigg\} \end{aligned} \tag{54}$$

where

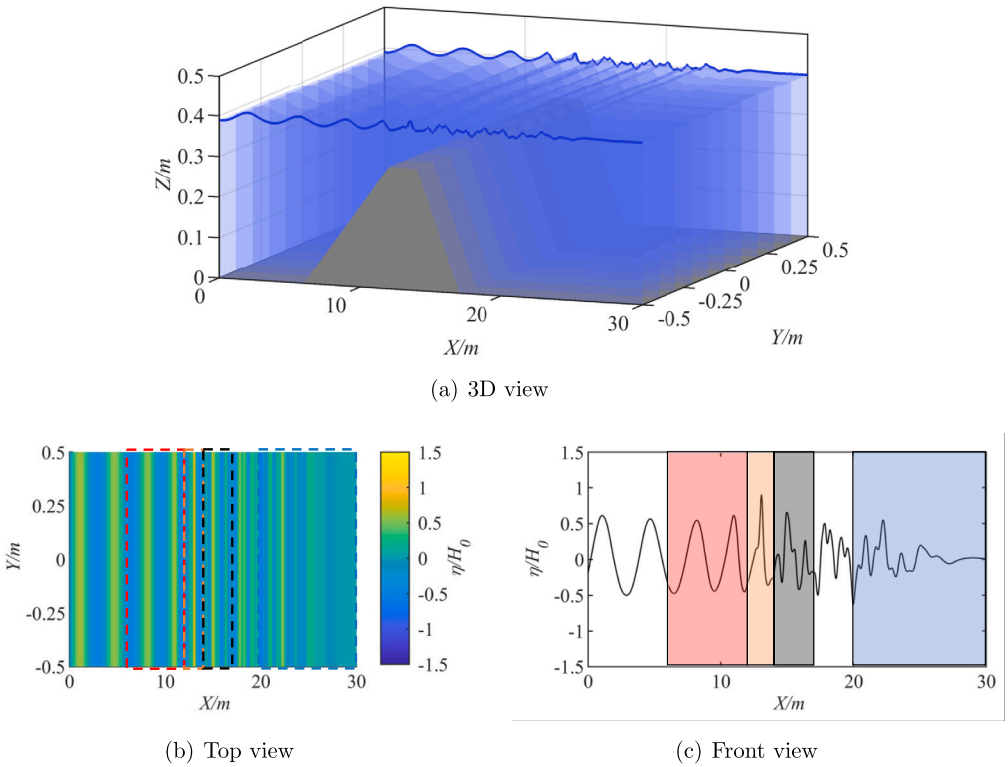

(a) 3D view

(b) Top view

(c) Front view

Fig. 9. The surface elevation of regular wave interacts with a submerged bar. (a) 3D view (b) Top view (c) Front view of free surface elevation changes at representative time (Red rectangle: 1:20 upslope; Yellow rectangle: horizontal crest; Black rectangle: 1:10 downslope; Blue rectangle: damping zone).

$$c = \frac{9\sqrt{\nu}}{2d\left(s + C_M\right)} \tag{55}$$

$$h = \frac{3}{2d\left(s + C_M\right)}\sqrt{\nu\left[8\left(s + C_M\right) - 9\right]} \tag{56}$$

$$\alpha = \tan^{-1}\left(\frac{h}{c}\right) \tag{57}$$

and $\mathrm{erfc}\,(t)$ is the complementary error function, which writes as:

$$\mathrm{erfc}\,(t) = \frac{2}{\sqrt{\pi}}\int_{\pi}^{\infty}\exp\left(-t^2\right)dt \tag{58}$$

Fig. 10(a) shows the comparison of analytical and numerical solutions of the motion of a 50 μm diameter sphere falling in water with the parameters $\rho_p = 2500\ \mathrm{kg}/m^3$, $s = \rho_p/\rho_f = 2.5$, kinematic viscosity $\nu = 10^{-6}\ m^2/s$ and particle Reynolds number $Re_p = 0.1$. As it takes very short time for a single particle to reach its terminal settling velocity, the time step is set as $\Delta t = 0.0001$ s. Significant differences can be observed when Basset force was considered or not. Without the Basset force, the particle reaches its settling velocity fast; while the particle accelerates at a much slower rate when Basset force is considered. It can also be clearly seen that the numerical results match well with the analytical solution.

As mentioned before, the analytical solution of the settling process of a round particle is only applicable to the linear (Stokes) drag law, experiments performed by Mordant et al. [70] are further adopted to validate the applicability of the point particle model in non-linear drag range. The sphere diameter used in the experiment is 500 μm, $s = \rho_p/\rho_f = 2.565$, $\nu = 9.0366 \times 10^{-7}\ m^2/s$, particle Reynolds number $Re_p = 41$ and the time step is set as $\Delta t = 0.00005$ s. It can be found from Fig. 10(b) that the numerical results match better with experimental data when the Basset force is considered. Both the early stage of particle settling and the terminal settling velocity correspond well to the experiments.

4.3. Benchmark: single particle in an oscillating liquid

Given the good agreement between our simulated settling process of a single particle in a stationary liquid, our attention now shifts to simulating settling process of a single particle in vertically oscillating liquid. The data are adapted from experiments done by

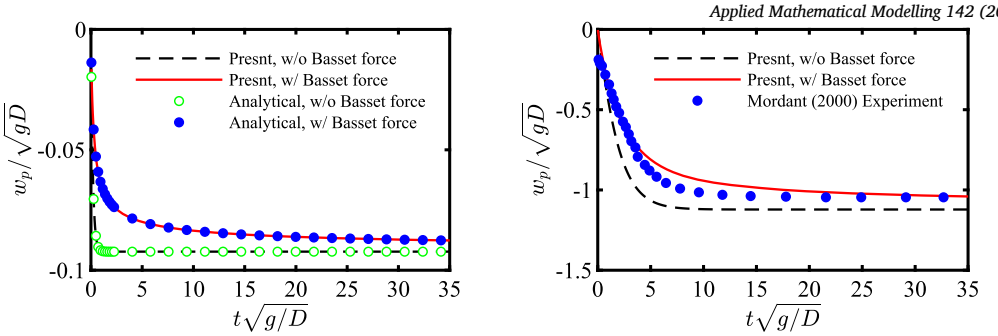

Fig. 10. Accelerated process of a spherical particle settle in a stationary liquid: (a) $Re_p = 0.1$; (b) $Re_p = 41$.

Table 3
Summary of different cases on sphere settling in oscillation field.

Case	Re_p	Diameter [μm]	ρ_p/ρ_f	Viscosity [10^{-6} m^2/s]	Oscillation period [s]	$\nu/d^2\omega_s$
1	0.18	1587	6.27	250.80	0.15	2.3
2	0.18	1587	6.27	250.80	0.19	3.0
3	1.1	3175	6.16	250.80	0.15	0.59
4	1.1	3175	6.16	250.80	0.19	0.74
5	6	1587	6.53	35.77	0.15	0.330
6	6	1587	6.53	35.77	0.19	0.430
7	28	3175	6.41	35.77	0.15	0.085
8	28	3175	6.41	35.77	0.19	0.110

Ho [71]. The experiments were conducted in a cylinder which was filled with fluids, and it would oscillate vertically with different amplitudes and frequencies as follows:

$$w_f(t) = w_{f0}\sin(\omega t) \tag{59}$$

where w_{f0} is the velocity oscillation amplitude; $\omega = 2\pi/T$ is the angular frequency and T is the oscillation period. The particle motion process is computed for several oscillation cycles until the velocity deviation between two consecutive periods is less than 0.1%. The average settling velocity ω_{sa} is computed by averaging the velocities in an oscillation cycle. The time step is set as $\Delta t = 0.00005$ s. Four different Re_p and two different oscillation periods are chosen. In total 8 cases are simulated. Detailed parameters used in the 8 cases are summarized in Table 3.

Fig. 11 shows the comparison between the simulated non-dimensional averaged settling velocity and oscillation acceleration ratio with experiments. The results depicted by the solid lines in Fig. 11 are obtained through a sequence of simulations, all maintaining the constant frequency while the wave amplitudes are systematically varied. Following these simulations, the oscillation acceleration ratios for each amplitude are computed and the relation between the wave amplitudes and the oscillation acceleration ratios are drawn into solid lines in this figure. It can be seen from these figures that with the increase of the oscillation amplitude, the non-dimensional averaged settling velocity would decrease. This reduction in settling velocity can be attributed to the enhanced particle inertia during the oscillating motion of the fluid, which, when increased, tends to overpower the effects of viscosity around the particle and can lead to a more distinct decrease in averaged settling velocity. Another interesting finding is that when the Basset force is considered in the settling process, the numerical simulation results deviate more than when the Basset force is not considered. One of the reasons lies in that the Basset force is applicable in relatively small particle Reynolds number and is inapplicable to high particle Reynolds number conditions [24]; Also the Basset force can be considered as a kind of viscous force and would resist the movement of the particle. As a result, the average settling velocity in one oscillation period would decrease when Basset force is considered. Finally, we can conclude that the numerical simulation results match better with experiments without Basset force. As the wave field can be seen as a specific oscillation flow, we would not consider the Basset force in our later simulation on sediment-laden jet in flow with waves.

4.4. Benchmark: sediment-laden jet in a stationary environment

To check the capability of the coupled model between the non-hydrostatic model and the point-particle model, we choose to simulate the sediment-laden jet in a stationary environment. The setup of the experiment is the same as the experiments performed by Chen et al. [72]. The tank has a length of 1.5 m, a width of 0.5 m, and a height of 0.6 m. The tank keeps a depth of 0.5 m. The diameter of the jet orifice is 0.01 m and is located 0.15 m above the collection tray. The computational domain is discretized into 131×41×139 grids. A non-uniform grid is implemented, and refined at the jet orifice, with minimum grid sizes in the x, y, and

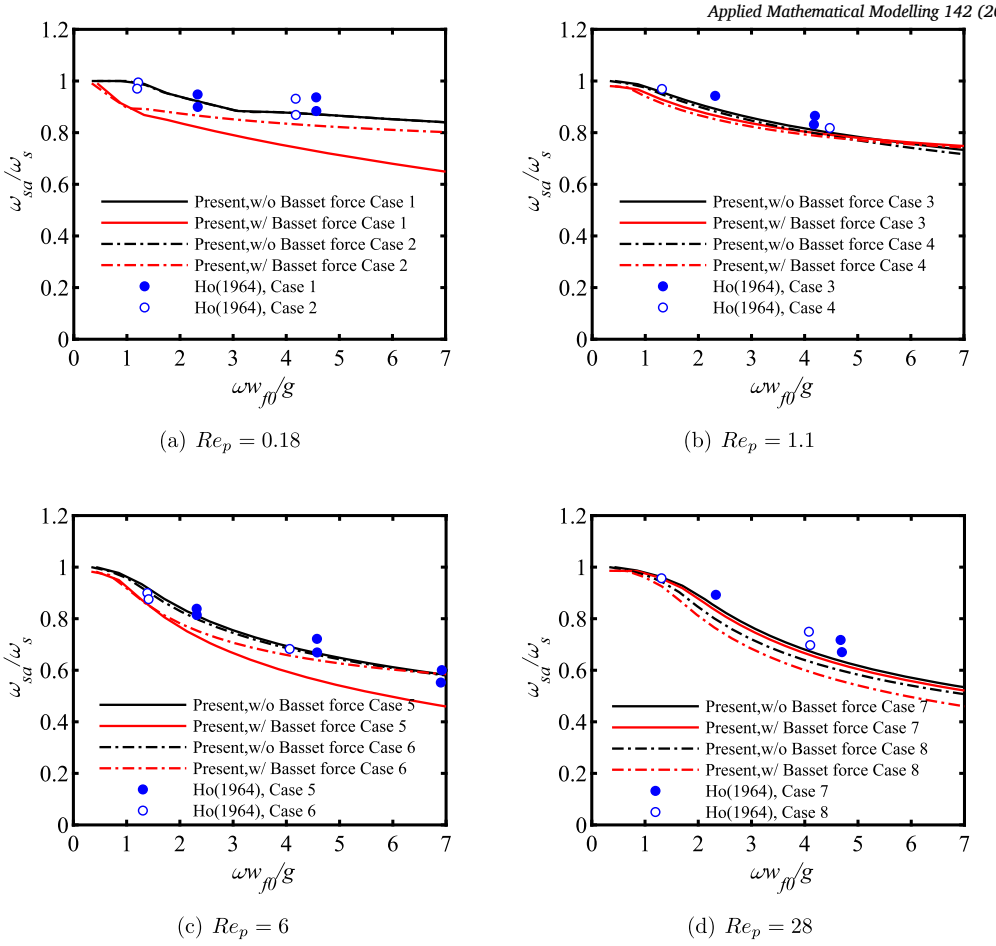

Fig. 11. Comparison of the numerical model and the experimental results of Ho [71] of accelerated process of a spherical particle settle in oscillation field.

σ directions of 0.001 m. The time step is set to 0.002 s and the total CPU time per time step required for the present model was approximately 4.3 s. The jet outlet velocity is set as 0.76 m/s and the velocity boundary is specified using the SEM (Synthetic-Eddy-Method) method. Given that the volume concentration of the simulated sediment-laden jet is below 0.1%, only one-way coupling is considered [73], where both the reaction of particles to the flow field and interactions among particles are neglected.

Fig. 12 shows the comparison of centerline velocity decay and axial velocity distribution between experimental and numerical results. To check the mesh convergence at the jet outlet boundary, the jet outlet was discretized by 8×8, 10×10 and 12×12 grids, respectively. It is found that the centerline velocity decay is similar when the jet outlet boundary is discretized by finer grids like Grid 10-10 and Grid 12-12. Therefore, the 10×10 grid was selected for the jet outlet boundary. Additionally, it is found that the simulation results match well with the experiments by Kwon and Seo [74]. When it comes to velocity distribution in cross-sections, it is found that the distribution follows the Gaussian distribution at cross-sections in self-similar zone. In conclusion, the accuracy of the flow field was verified.

We present 3D visualizations of the instantaneous and time-averaged isosurfaces of a jet in a stationary environment (see Fig. 13). The isosurfaces represent velocities ranging from 0.2 m/s to 0.8 m/s, with intervals of 0.2 m/s. Fig. 13(a) shows the velocity distribution of the jet at a specific time, where the isosurface appears irregular, reflecting the fluctuating structures caused by the inherent unsteadiness and turbulence of the flow. In contrast, the time-averaged velocity isosurface (see Fig. 13(b)) appears smoother than the instantaneous one. The shapes and behavior of both instantaneous and time-averaged isosurfaces are consistent with previous studies on turbulent jets in stationary environments, thereby validating the accuracy of the numerical simulation model.

The particles used in the numerical simulation have a median size D_{50} = 200 μm. As shown in Fig. 14(a), the actual diameter distribution follows the distributions used in experiments, which was measured using the Laser Diffraction Particle Size Analyzer (Malvern Mastersizer 3000). A total of 8 different kinds of particle diameters are used in the simulation. Particles were put into different grid cells on the jet outlet boundary. A Gaussian white noise is applied to determine the precise time step for particle release from the jet boundary as particles do not exit each grid cell at every time step. This initial artificial asymmetry in particle distribution can be quickly dissipated by turbulence as the jet flow develops downstream, having minimal impact on the final results [75].

The 1-D deposition pattern is shown in Fig. 14(b). To ensure the repeatability and avoid the effect of noise in particle numbers on the final deposition pattern, two different particle numbers namely 81000 and 162000 particles are adopted in the numerical

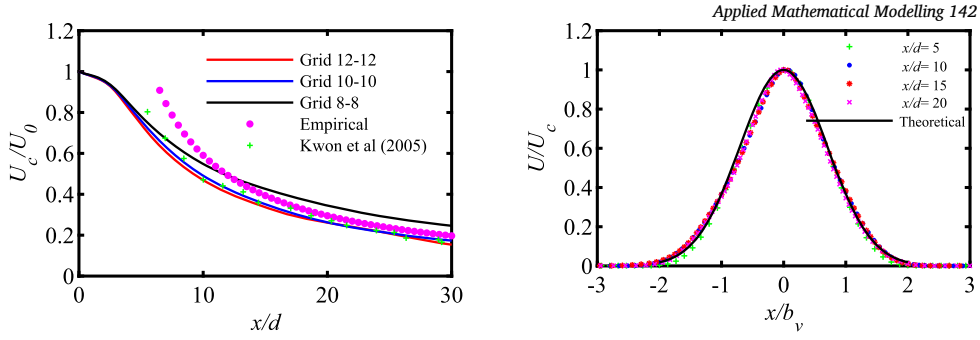

(a) centerline velocity decay (b) axial velocity distribution

Fig. 12. Comparison of (a) centerline velocity decay with different grids; (b) axial velocity distribution (b_v means jet Gaussian half-width) between experiments and numerical simulation.

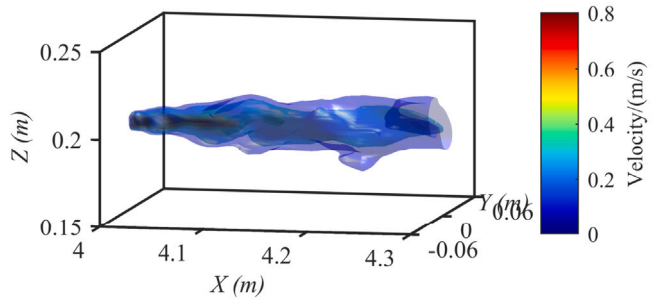

(a) Instantaneous velocity isosurface

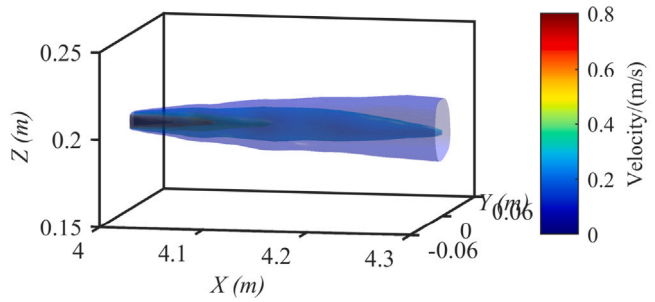

(b) Time-averaged velocity isosurface

Fig. 13. Comparison of (a) instantaneous and (b) time-averaged velocity isosurfaces of the jet in a stationary environment, with isosurfaces shown at velocity magnitudes of 0.2 m/s to 0.8 m/s, in 0.2 m/s increments.

simulation. It can be seen from the figure that the simulated 1-D deposition pattern matches well with the experiments. The deposition pattern shares great similarity when using 81000 or 162000 particles. Therefore, the number of sediment particles is set to 81000 hereafter to reduce computational cost.

The two-dimensional deposition pattern is shown in Fig. 15. The black contour lines are the 2-D deposition concentration which equals the deposition rate divided by the bottom grid size. The profiles are consistent with the previously measured 1-D deposition profiles, with a peak deposition at about 0.2 m from the jet orifice for this case. It can also be seen that the sediment deposition would expand, and deposition patterns are almost symmetric.

Fig. 16 shows the three-dimensional visualization of a horizontal sediment-laden jet in a stationary environment. The positions of the sediment particles are marked as spheres, while their instantaneous velocities are distinguished by various colors. The visualization clearly shows that sediments initially follow the flow movement in the near field. As the flow velocity decreases downstream, the sediments would gradually deviate from the jet centerline (i.e., $z = 0.18$ m) and move downward due to gravity. Consequently, fewer sediments are observed in the upper part of the jet cross-sections (i.e., $z > 0.18$ m) and hardly can sediment be seen in the upper part of jet far field (i.e., $x > 0.6$ m).

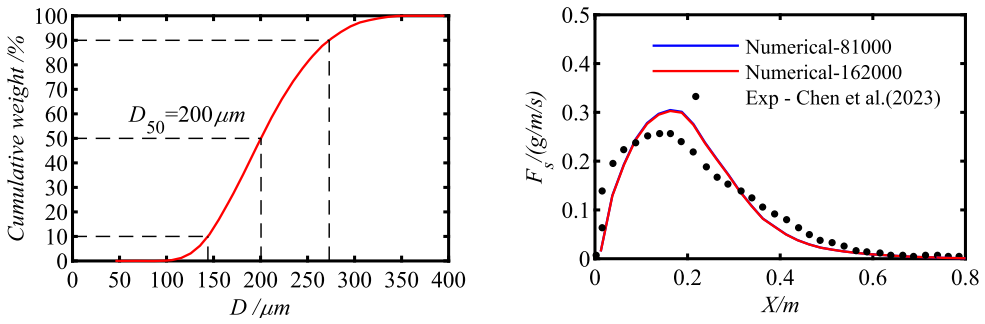

(a) Particle diameter distribution (b) 1-D deposition pattern

Fig. 14. Verification of sediment-laden jet in an initially stationary environment: (a) particle diameter distribution; (b) 1-D deposition pattern.

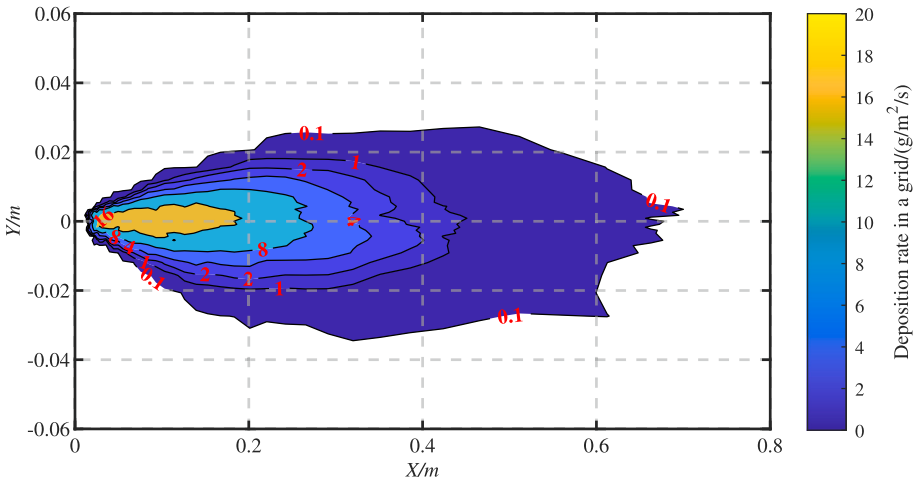

Fig. 15. 2-D deposition pattern of sediment-laden jet in an initially stationary environment (Top View).

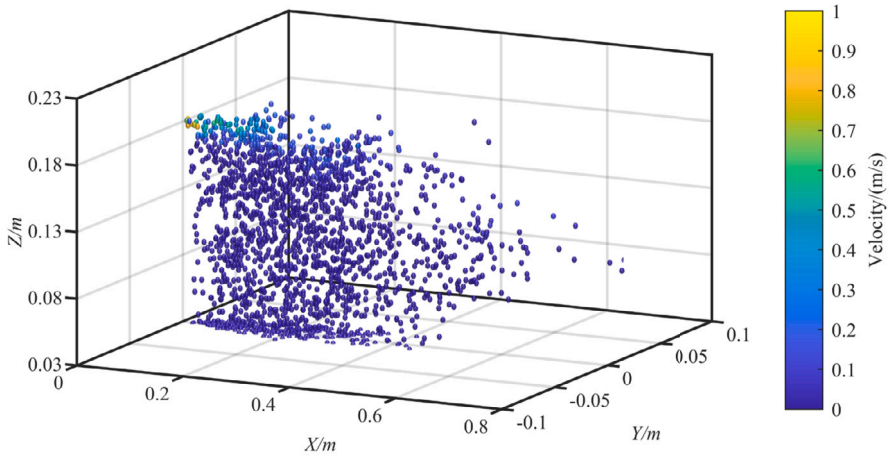

Fig. 16. 3-D visualization of sediment-laden jet in an initially stationary environment.

4.5. Benchmark: sediment-laden jet in flow with waves

Finally, we further use this model to simulate a sediment-laden jet in flow with waves. The experiments were carried out within a wave flume located at the College of Harbor, Coastal and Offshore Engineering, Hohai University. Fig. 17 shows a sketch of the experimental setup. The flume dimensions were 46 m in length, 0.5 m in width, and 1.0 m in depth. All experiments consisted of four

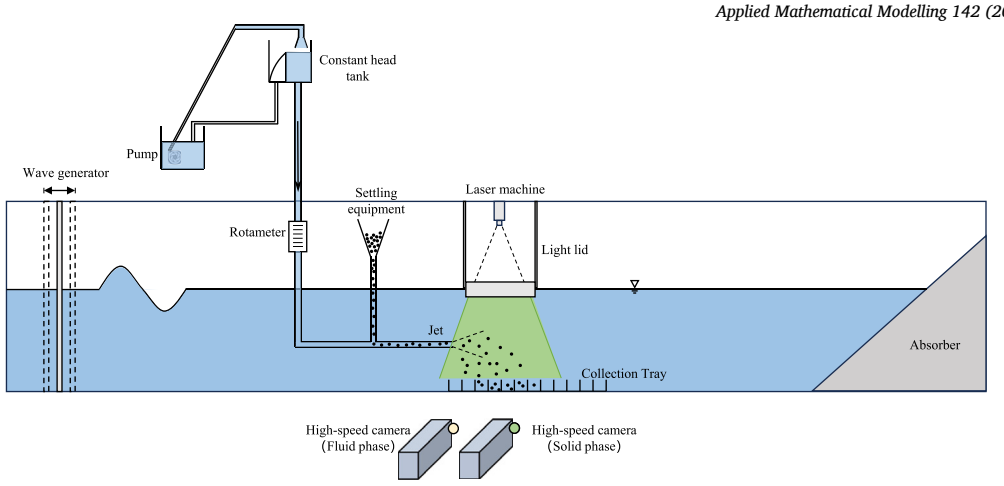

Fig. 17. Experimental set up.

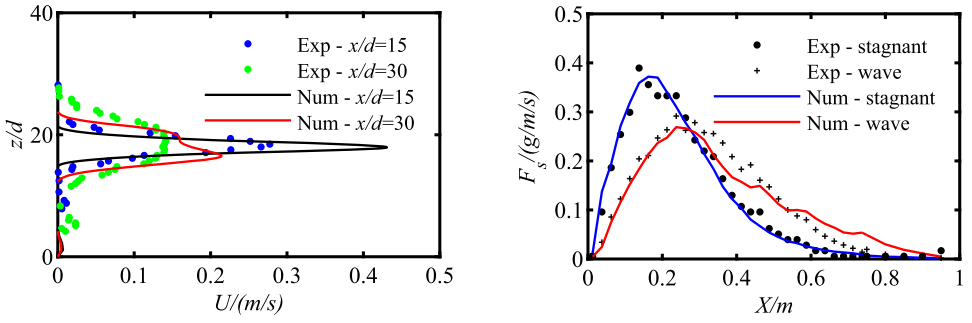

(a) flow verification (b) 1-D deposition pattern

Fig. 18. Comparison of the numerical model and the experimental results of sediment-laden jet in flow with waves, (a) flow field; (b) 1-D deposition pattern.

systems, namely the wave generating system, the sediment-laden jet generating system, the measuring system, and the collection system. The wave generating system consisted of a wave paddle and an absorber. This system was used to make regular waves. The sediment-laden jet generating system mainly consisted of a constant head tank which was full of feeding particles and settling equipment to feed sediment into the flow. The measuring system consisted of a continuous laser machine and two high-speed cameras, which made it into a PIV system. Finally, the collection tray was used to collect all the settled sediment. A horizontal jet was introduced through an acrylic nozzle with a diameter of 0.01 m. The nozzle was positioned at the flume's midpoint, maintaining a 0.18 m clearance above the bottom. To maintain a consistent exit velocity, water was continuously pumped at a constant head, while the discharge rate was controlled by a rotameter. The wave height was 0.022 m and the wave period was set as 1.5 s. To fix the jet position in flow with waves, a double-layer σ coordinate [76] is adopted in the simulation. The computational domain is 15 m in length, 0.5 m in width, 0.5 m in depth and is discretized by 368×41×139 grids. A non-uniform grid is employed and refined at the jet orifice, with minimum grid sizes in the x, y, and σ directions of 0.1 m. The time step is set to 0.002 s and the total CPU time per time step required for the present model was about 10.2 s. The jet outlet velocity is set as 0.85 m/s. As it was found in the former section the number of sediment particles has no impact on the final deposition outcome once it exceeds 81000, the number of particles is set to be 81000 and these particles are injected at each grid on the jet outflow boundary.

Fig. 18(a) shows the comparison of the velocity distribution of horizontal jet under wave conditions between experimental data and numerical results at $x/d = 15$ and $x/d = 30$. It suggests that the simulated velocity profiles have the same trend as that in the experiments but the values are over-predicted. The main reason for this outcome is that, in the experiments, the elevation inside the sediment-feeding system would change in accordance with the outside elevation changes due to the existence of waves. As a result, the outflow velocity near the jet orifice varies within a wave cycle. Therefore, an extra oscillation velocity should be added to the jet outlet velocity. However, this simulation does not consider such specific phenomena. Nonetheless, the velocity remains consistent with the experimental data.

Fig. 18(b) shows the 1-D deposition pattern of the horizontal sediment-laden jet in flow with waves and initially stationary water. The results indicate that the simulated deposition aligns closely with experimental data, except in the relatively far field

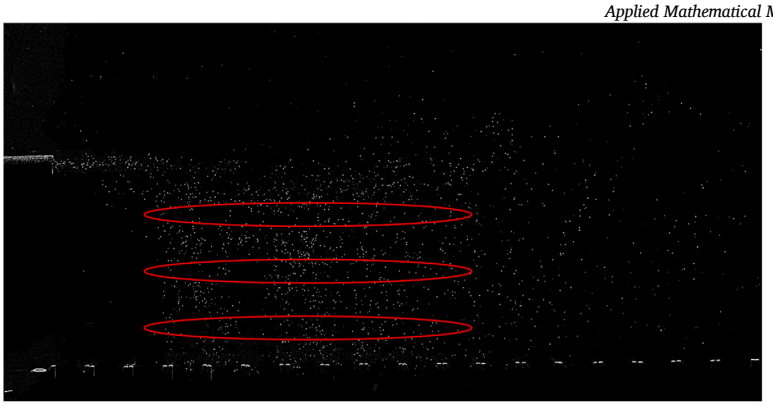

(a) Experiment - original image

(b) Experiment - invert the grayscale of the original image

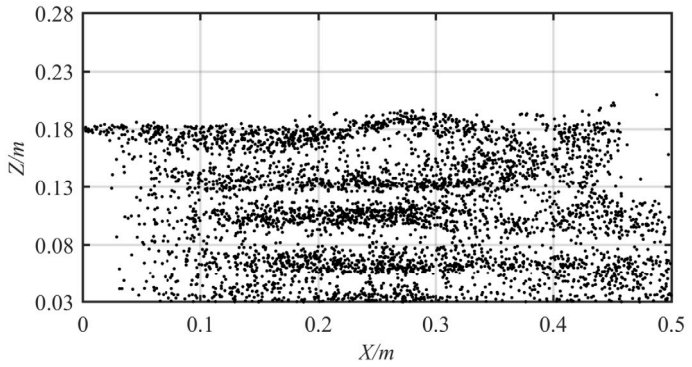

(c) Numerical

Fig. 19. Comparison of instantaneous sediment distribution between the numerical model and the experimental results of sediment-laden jet at wave peak phase.

where increased sediment deposition is observed when compared to that in the experiments. This discrepancy may be due to the comparatively high outflow velocity used in our simulation. In addition, compared with the sediment-laden jet in initially stationary water, it is found that the deposition rate decreases in the near field while a higher deposition rate is observed in the middle and far-field when the sediment-laden jet is injected under wavy conditions, which are well captured by the model.

The comparison of instantaneous sediment distribution between the numerical model and the experimental results of the sediment-laden jet at wave peak phase is shown in Fig. 19. Fig. 19(a) shows the original experimental image, while Fig. 19(b) presents the same image with an inverted grayscale for better comparison with numerical simulation results. Obvious discontinuities in sediment deposition which are marked in red ellipses can be seen in Fig. 19(b). The discontinuities also show periodic changes, which are likely to be attributed to the impact of the wave. The numerical results capture the overall pattern well. In positions closer to the bottom, discontinuities remain clearly visible in our model, whereas they are hardly to be observed in the experiments. The main reason is

that the sediment particles adopted in our model are chosen to have the same diameter, which is different from the experiments. Consequently, once the particles leave the jet body, they tend to move at the same speed due to uniform settling velocities. As a result, discontinuities remain clearly visible in our model even in areas close to the bottom.

A set of three-dimensional visualizations of the horizontal sediment-laden jet at different wave phases are shown in Fig. 20. It can be seen that particles would sway upward and downward under wave conditions, which is the most distinctive deposition pattern compared to the initially stationary case. Additionally, the visualizations also reveal that particles are transported further under the effect of waves. Fig. 21 shows the two-dimensional (2-D) deposition pattern of the sediment-laden jet under wave conditions. The 2-D sediment concentration contour lines cover a confined area with higher deposition rates, specifically when the deposition rate in a grid is larger than 16 $g/m^2/s$; whereas they cover a broader area in smaller values like when the deposition rate in a grid is less than 1 $g/m^2/s$. In summary, the model captures the behavior of the horizontal sediment-laden jet under wave conditions.

5. Conclusion

This paper introduces a two-phase flow model that couples the non-hydrostatic model with the point-particle model to simulate sediment-laden flow problems associated with temporal changes in the free surface. A Lagrangian-Eulerian method is utilized to track the free surface, and the movement of sediment particles is tracked by a point-particle model. The model's accuracy is validated through comparison with five distinct cases.

First, the propagation of regular waves at a constant depth is simulated using this model. It is found that both the free surface and flow fields match well with analytical solutions. The model is then extended to address varying water depth scenarios, specifically the interaction of regular waves with a submerged bar. The numerical results also correspond well with experimental findings. This underscores the model's effectiveness in simulating behavior related to changes in free surface. After that, the verification of the point-particle model is conducted. The deposition processes of a single particle, both in stationary and oscillating environments are simulated, yielding results that closely match with analytical solutions and experimental data. Finally, the two-phase flow model, integrated with the point-particle model, is employed to simulate a dilute horizontal sediment-laden jet in both stationary and wave environments. The observed deposition patterns are found to be in line with experimental outcomes, affirming the model's capability to accurately represent sediment transport processes.

The new model shows significant potential as a numerical tool for simulating sediment-laden free surface flows. Currently, the point-particle model is limited to one-way coupling with the flow, where the reaction force of particles on the flow and the collisions between particles are not considered. This limitation makes it primarily suitable for low-concentration sediment-laden flows. In the future, the reaction force of particles on the flow will be incorporated into the governing equation as a source term, and either the soft-sphere [77] model or hard-sphere model [78] will be employed for the dispersed phase to simulate problems with higher sediment concentrations.

CRediT authorship contribution statement

Yuhang Chen: Writing – original draft, Visualization, Validation, Software, Methodology, Investigation, Formal analysis, Data curation. **Yongping Chen:** Writing – review & editing, Supervision, Software, Project administration, Methodology, Investigation, Funding acquisition, Formal analysis, Conceptualization. **Zhenshan Xu:** Supervision, Software, Investigation, Funding acquisition. **Pengzhi Lin:** Writing – review & editing, Software, Methodology, Investigation, Formal analysis. **Zhihua Xie:** Writing – review & editing, Supervision, Resources, Investigation, Funding acquisition, Formal analysis, Conceptualization.

Declaration of competing interest

The authors declare that they have no known competing financial interests or personal relationships that could have appeared to influence the work reported in this paper.

Acknowledgements

This work was supported by the National Key Research and Development Program of China (2023YFC3008100), the National Natural Science Foundation of China (51979076, 52211530103) and United Kingdom Engineering and Physical Sciences Research Council (EPSRC) grant (EP/V040235/1). The first author also would like to acknowledge the financial support from the China Scholarship Council (CSC) under PhD exchange program at Cardiff University [202206710100]. Constructive comments from anonymous reviewers have helped to improve the manuscript and these are gratefully acknowledged. Special thanks are also given to editors for their meticulous handling of the manuscript and dedication throughout the review process, which has significantly enhanced the readability and overall quality of this work.

Data availability

Data will be made available on request.

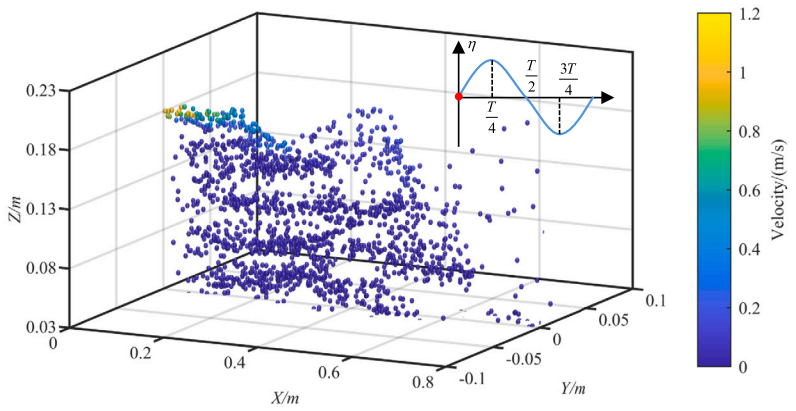

(a) Wave up-crossing

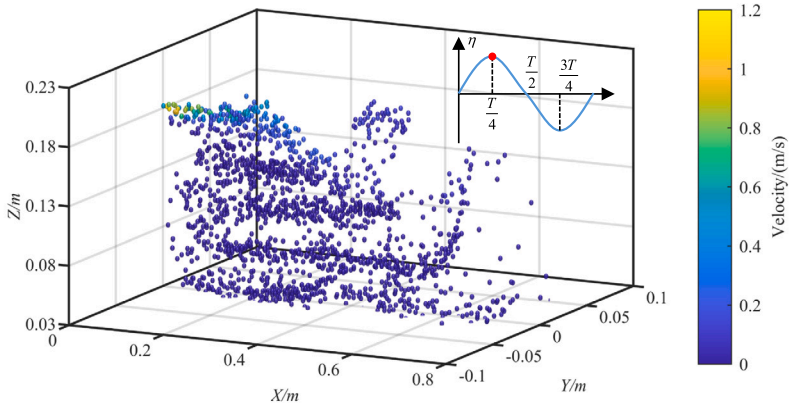

(b) Wave peak

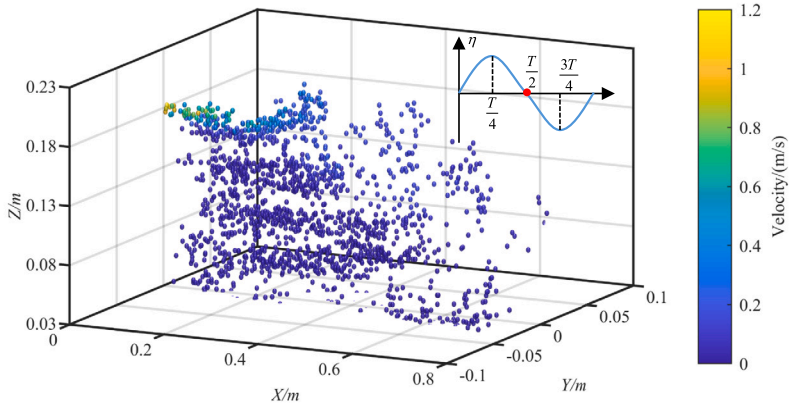

(c) Wave down-crossing

Fig. 20. 3-D visualization of initial stage of sediment-laden jet in flow with waves at four different wave phases (a) Wave up-crossing, (b) Wave peak, (c) Wave down-crossing and (d) Wave trough.

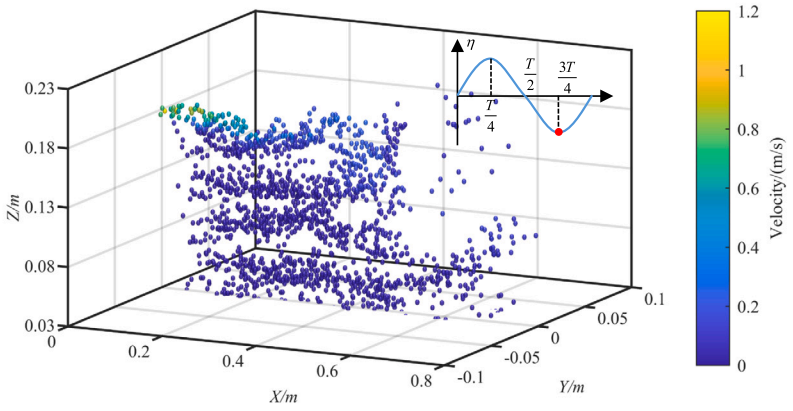

(d) Wave trough

Fig. 20. (*continued*)

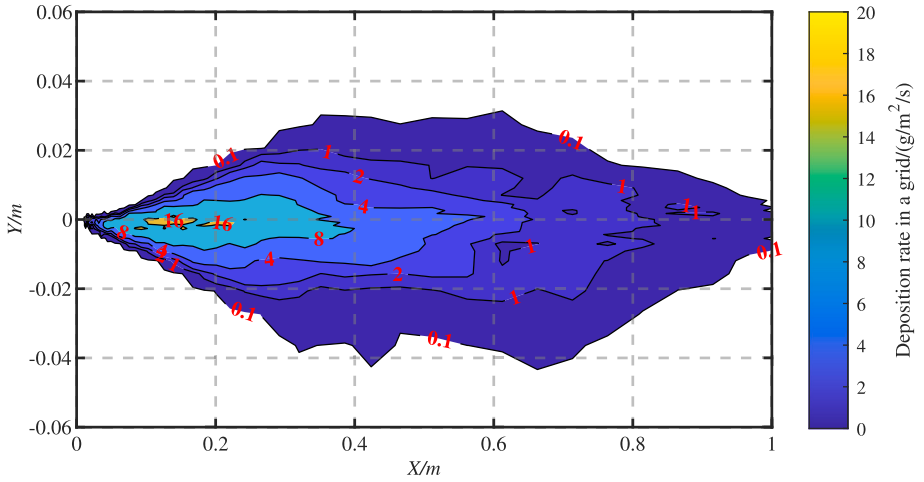

Fig. 21. 2-D deposition pattern of sediment-laden jet in flow with waves.

References

[1] D.J. Piper, P. Cochonat, M.L. Morrison, The sequence of events around the epicentre of the 1929 grand banks earthquake: initiation of debris flows and turbidity current inferred from sidescan sonar, Sedimentology 46 (1999) 79–97.
[2] J. Syvitski, J.R. Ángel, Y. Saito, I. Overeem, C.J. Vörösmarty, H. Wang, D. Olago, Earth's sediment cycle during the Anthropocene, Nature Rev. Earth Environ. 3 (2022) 179–196.
[3] J.L. Li, G.X. Wang, C.L. Song, S.Q. Sun, J.P. Ma, Y. Wang, L.M. Guo, D.F. Li, Recent intensified erosion and massive sediment deposition in Tibetan Plateau rivers, Nat. Commun. 15 (2024) 722.
[4] J.K. Reece, R.M. Dorrell, K.M. Straub, Circulation of hydraulically ponded turbidity currents and the filling of continental slope minibasins, Nat. Commun. 15 (2024) 2075.
[5] E. Stokstad, Prospect of unregulated deep-sea mining looms, Science 381 (2023) 254–255.
[6] P.J. Talling, S. Hage, M.L. Baker, T.S. Bianchi, R.G. Hilton, K.L. Maier, The global turbidity current pump and its implications for organic carbon cycling, Annu. Rev. Mar. Sci. 16 (2024) 105–133.
[7] P. Dong, K.F. Zhang, Two-phase flow modelling of sediment motions in oscillatory sheet flow, Coast. Eng. 36 (1999) 87–109.
[8] T.-J. Hsu, J.T. Jenkins, P.L.-F. Liu, On two-phase sediment transport: sheet flow of massive particles, Proc. R. Soc. Lond., Ser. A, Math. Phys. Eng. Sci. 460 (2004) 2223–2250.
[9] L. Amoudry, T.-J. Hsu, P.-F. Liu, Two-phase model for sand transport in sheet flow regime, J. Geophys. Res., Oceans 113 (2008).
[10] T. Revil-Baudard, J. Chauchat, A two-phase model for sheet flow regime based on dense granular flow rheology, J. Geophys. Res., Oceans 118 (2013) 619–634.
[11] Z. Cheng, T.-J. Hsu, J. Calantoni, Sedfoam: a multi-dimensional Eulerian two-phase model for sediment transport and its application to momentary bed failure, Coast. Eng. 119 (2017) 32–50.
[12] A. Mathieu, Z. Cheng, J. Chauchat, C. Bonamy, T.-J. Hsu, Numerical investigation of unsteady effects in oscillatory sheet flows, J. Fluid Mech. 943 (2022) A7.
[13] I. Vinkovic, D. Doppler, J. Lelouvetel, M. Buffat, Direct numerical simulation of particle interaction with ejections in turbulent channel flows, Int. J. Multiph. Flow 37 (2011) 187–197.
[14] R. Sun, H. Xiao, CFD-DEM simulations of current-induced dune formation and morphological evolution, Adv. Water Resour. 92 (2016) 228–239.

[15] D. Wildt, C. Hauer, H. Habersack, M. Tritthart, LES two-phase modelling of suspended sediment transport using a two-way coupled Euler–Lagrange approach, Adv. Water Resour. 160 (2022) 104095.
[16] J.F. Xie, P. Hu, C.L. Zhu, Z.S. Yu, T. Pähtz, Turbidity currents propagating down an inclined slope: particle auto-suspension, J. Fluid Mech. 954 (2023) A44.
[17] A. Shakibaeinia, Y.-C. Jin, MPS mesh-free particle method for multiphase flows, Comput. Methods Appl. Math. 229 (2012) 13–26.
[18] C. Ulrich, M. Leonardi, T. Rung, Multi-physics SPH simulation of complex marine-engineering hydrodynamic problems, Ocean Eng. 64 (2013) 109–121.
[19] Q.H. Ran, J. Tong, S.D. Shao, X.D. Fu, Y.P. Xu, Incompressible SPH scour model for movable bed dam break flows, Adv. Water Resour. 82 (2015) 39–50.
[20] H.B. Shi, X.P. Yu, R.A. Dalrymple, Development of a two-phase SPH model for sediment laden flows, Comput. Phys. Commun. 221 (2017) 259–272.
[21] M.A. Nabian, L. Farhadi, Multiphase mesh-free particle method for simulating granular flows and sediment transport, J. Hydraul. Eng. 143 (2017) 04016102.
[22] M. Wang, Y. Pan, X. Shi, J. Wu, P. Sun, Comparative study on volume conservation among various sph models for flows of different levels of violence, Coast. Eng. 191 (2024) 104521.
[23] J.R. Finn, M. Li, S.V. Apte, Particle based modelling and simulation of natural sand dynamics in the wave bottom boundary layer, J. Fluid Mech. 796 (2016) 340–385.
[24] M.R. Maxey, J.J. Riley, Equation of motion for a small rigid sphere in a nonuniform flow, Phys. Fluids 26 (1983) 883–889.
[25] C.S. Peskin, Flow Patterns Around Heart Valves: a Digital Computer Method for Solving the Equations of Motion, Yeshiva Univ., 1972.
[26] M. Uhlmann, An immersed boundary method with direct forcing for the simulation of particulate flows, J. Comput. Phys. 209 (2005) 448–476.
[27] A.G. Kidanemariam, M. Uhlmann, Direct numerical simulation of pattern formation in subaqueous sediment, J. Fluid Mech. 750 (2014) R2.
[28] M. Uhlmann, Interface-resolved direct numerical simulation of vertical particulate channel flow in the turbulent regime, Phys. Fluids 20 (2008).
[29] A. Prosperetti, Life and death by boundary conditions, J. Fluid Mech. 768 (2015) 1–4.
[30] Z. Jiang, P. Haff, Multiparticle simulation methods applied to the micromechanics of bed load transport, Water Resour. Res. 29 (1993) 399–412.
[31] M.A. van der Hoef, M. van Sint Annaland, N. Deen, J. Kuipers, Numerical simulation of dense gas-solid fluidized beds: a multiscale modeling strategy, Annu. Rev. Fluid Mech. 40 (2008) 47–70.
[32] S. Apte, K. Mahesh, T. Lundgren, Accounting for finite-size effects in simulations of disperse particle-laden flows, Int. J. Multiph. Flow 34 (2008) 260–271.
[33] J. Capecelatro, O. Desjardins, Eulerian–Lagrangian modeling of turbulent liquid–solid slurries in horizontal pipes, Int. J. Multiph. Flow 55 (2013) 64–79.
[34] A. Hager, C. Kloss, S. Pirker, C. Goniva, Parallel resolved open source CFD-DEM: method, validation and application, J. Comput. Multiph. Flows 6 (2014) 13–27.
[35] C.W. Hirt, B.D. Nichols, Volume of Fluid (VOF) method for the dynamics of free boundaries, J. Comput. Phys. 39 (1981) 201–225.
[36] T. Shan, J.D. Zhao, A coupled CFD-DEM analysis of granular flow impacting on a water reservoir, Acta Mech. 225 (2014) 2449–2470.
[37] L. Jing, C. Kwok, Y.F. Leung, Y. Sobral, Extended CFD–DEM for free-surface flow with multi-size granules, Int. J. Numer. Anal. Methods Geomech. 40 (2016) 62–79.
[38] Z.H. Shen, G. Wang, D.R. Huang, F. Jin, A resolved CFD-DEM coupling model for modeling two-phase fluids interaction with irregularly shaped particles, J. Comput. Phys. 448 (2022) 110695.
[39] W.X. Li, H.B. Shi, X.P. Yu, A DEM-based Euler–Lagrange model for motion of particle–fluid two-phase mixtures, Acta Geotech. (2023) 1–19.
[40] C.F. Ai, Y.X. Ma, C.F. Yuan, G.H. Dong, A 3D non-hydrostatic model for wave interactions with structures using immersed boundary method, Comput. Fluids 186 (2019) 24–37.
[41] P.Z. Lin, C.W. Li, A σ-coordinate three-dimensional numerical model for surface wave propagation, Int. J. Numer. Methods Fluids 38 (2002) 1045–1068.
[42] G.F. Ma, F.Y. Shi, J.T. Kirby, Shock-capturing non-hydrostatic model for fully dispersive surface wave processes, Ocean Model. 43 (2012) 22–35.
[43] M. Zijlema, G.S. Stelling, Further experiences with computing non-hydrostatic free-surface flows involving water waves, Int. J. Numer. Methods Fluids 48 (2005) 169–197.
[44] M. Zijlema, G. Stelling, Efficient computation of surf zone waves using the nonlinear shallow water equations with non-hydrostatic pressure, Coast. Eng. 55 (2008) 780–790.
[45] C.F. Ai, S. Jin, B. Lv, A new fully non-hydrostatic 3D free surface flow model for water wave motions, Int. J. Numer. Methods Fluids 66 (2011) 1354–1370.
[46] Y.P. Chen, C.W. Li, C.K. Zhang, Numerical modeling of a round jet discharged into random waves, Ocean Eng. 35 (2008) 77–89.
[47] Z.S. Xu, Y.P. Chen, J.F. Tao, Y. Pan, D.M. Sowa, C.W. Li, Three-dimensional flow structure of a non-buoyant jet in a wave-current coexisting environment, Ocean Eng. 116 (2016) 42–54.
[48] Z.S. Xu, Y.P. Chen, Y.N. Wang, C.K. Zhang, Near-field dilution of a turbulent jet discharged into coastal waters: effect of regular waves, Ocean Eng. 140 (2017) 29–42.
[49] Z.S. Xu, Y.P. Chen, Y. Pan, Initial dilution equations for wastewater discharge: example of non-buoyant jet in wave-following-current environment, Ocean Eng. 164 (2018) 139–147.
[50] G. Ma, J.T. Kirby, F. Shi, Numerical simulation of tsunami waves generated by deformable submarine landslides, Ocean Model. 69 (2013) 146–165.
[51] N.A. Berard, R.P. Mulligan, A.M.F. da Silva, M. Dibajnia, Evaluation of XBeach performance for the erosion of a laboratory sand dune, Coast. Eng. 125 (2017) 70–80.
[52] C. Zhang, J.T. Kirby, F.Y. Shi, G.F. Ma, S.T. Grilli, A two-layer non-hydrostatic landslide model for tsunami generation on irregular bathymetry. 2. Numerical discretization and model validation, Ocean Model. 160 (2021) 101769.
[53] J. Smagorinsky, General circulation experiments with the primitive equations: I. The basic experiment, Mon. Weather Rev. 91 (1963) 99–164.
[54] P. Lin, Numerical Modeling of Water Waves, CRC Press, 2008.
[55] P.Z. Lin, P.L.-F. Liu, A numerical study of breaking waves in the surf zone, J. Fluid Mech. 359 (1998) 239–264.
[56] J. Mani, S. Jayakumar, Wave transmission by suspended pipe breakwater, J. Waterw. Port Coast. Ocean Eng. 121 (1995) 335–338.
[57] S. Neelamani, R. Rajendran, Wave interaction with t-type breakwaters, Ocean Eng. 29 (2002) 151–175.
[58] X. Yu, Diffraction of water waves by porous breakwaters, J. Waterw. Port Coast. Ocean Eng. 121 (1995) 275–282.
[59] J.C. Park, M.H. Kim, H. Miyata, Fully non-linear free-surface simulations by a 3D viscous numerical wave tank, Int. J. Numer. Methods Fluids 29 (1999) 685–703.
[60] N. Jarrin, S. Benhamadouche, D. Laurence, R. Prosser, A synthetic-eddy-method for generating inflow conditions for large-eddy simulations, Int. J. Heat Fluid Flow 27 (2006) 585–593.
[61] Z.M. Lu, M.Z. Yuan, The LDA measurement of turbulent flow in square duct and the comparison of some flow characteristics with pipe flow, Acta Mech. Sin. 18 (1986).
[62] X.H. Wu, P. Moin, A direct numerical simulation study on the mean velocity characteristics in turbulent pipe flow, J. Fluid Mech. 608 (2008) 81–112.
[63] C.W. Li, T. Yu, Numerical investigation of turbulent shallow recirculating flows by a quasi-three-dimensional $k-\epsilon$ model, Int. J. Numer. Methods Fluids 23 (1996) 485–501.
[64] N.N. Janenko, The Method of Fractional Steps, vol. 160, Springer, 1971.
[65] L. Zhu, C.W. Li, Error study on numerical approximation of radiation boundary condition for one-dimensional wave equation, Commun. Numer. Methods Eng. 9 (1993) 475–482.
[66] Y.P. Chen, C.W. Li, C.K. Zhang, Development of a fully nonlinear numerical wave tank, China Ocean Eng. 18 (2004) 501–514.
[67] S.N. Chan, Mixing and deposition of sediment-laden buoyant jets, HKU Theses Online (HKUTO), 2013.
[68] S. Beji, J. Battjes, Experimental investigation of wave propagation over a bar, Coast. Eng. 19 (1993) 151–162.
[69] L.M. Brush Jr, H.-W. Ho, B.-C. Yen, Accelerated motion of a sphere in a viscous fluid, J. Hydr. Eng. Div. 90 (1964) 149–160.
[70] N. Mordant, J.-F. Pinton, Velocity measurement of a settling sphere, Eur. Phys. J. B 18 (2000) 343–352.

[71] H.-W. Ho, Fall Velocity of a Sphere in a Field of Oscillating Fluid, The Univ. of Iowa, 1964.
[72] Y.P. Chen, E. Otoo, Y.H. Chen, Z.S. Xu, X.F. Li, Y. Zhou, Deposition behaviour of inclined momentum sediment-laden jet, Ocean Eng. 278 (2023) 114399.
[73] L. Brandt, F. Coletti, Particle-laden turbulence: progress and perspectives, Annu. Rev. Fluid Mech. 54 (2022) 159–189.
[74] S.J. Kwon, I.W. Seo, Reynolds number effects on the behavior of a non-buoyant round jet, Exp. Fluids 38 (2005) 801–812.
[75] P. Liu, K.M. Lam, Large-eddy simulation of horizontally discharging sediment-laden jets, J. Hydro-Environ. Res. 9 (2015) 388–403.
[76] Y. Chen, Y. Chen, Z. Xu, P. Lin, Z. Xie, A double-layer non-hydrostatic model for simulating wave-structure and wave-jet interactions, J. Comput. Phys. 523 (2025) 113634.
[77] P.A. Cundall, O.D. Strack, A discrete numerical model for granular assemblies, Geotechnique 29 (1979) 47–65.
[78] H.P. Zhu, Z.Y. Zhou, R. Yang, A. Yu, Discrete particle simulation of particulate systems: theoretical developments, Chem. Eng. Sci. 62 (2007) 3378–3396.